Fault zone deformation in welded tuffs at Yucca Mountain, Nevada

Mary Beth Gray[a], John A. Stamatakos[b], David A., Ferrill[b], Mark A. Evans[c], Brad Jordan[a]

[a] *Department of Geology, Bucknell University, Lewisburg, PA 17837*

[b] *Center for Nuclear Waste Regulatory Analyses, Southwest Research Institute, San Antonio, TX 78238*

[c] *Department of Geology and Planetary Sciences, University of Pittsburgh, Pittsburgh, PA 15260*

Abstract

Field and microstructural analysis of faults with millimeters to 100's of meters displacement within Yucca Mountain has led to identification of four distinctive fault architectural styles (Classes A, B, C, and D). Three of these classes of faults are genetically related. Differences in morphology and deformation mechanisms are related to differences in displacement and changes in the rheology of fault rocks. These faults formed by progressive cataclasis, leading to (at highest displacement) the development of a foliated gouge core and wide damage zone. One set of faults (Class B) however, is unique, having a different average orientation, mineralogy, microtexture, and gross architecture. Unlike other faults, puzzle-piece breccia cores consisting of >65% calcite indicates that Class B faults have strong dilational components and formed under fluid saturated conditions. Paleotemperature, isotopic signature, and morphology of secondary mineralization in Class B faults indicate that at some undetermined time in the history of Yucca Mountain, fluid fluxes were sufficient to develop these secondary minerals within the Class B faults. Comparisons to other occurrences of secondary minerals within open lithophysal cavities lead us to suggest that the secondary mineralization history at Yucca Mountain was complex and polygenetic. The age and origin of the secondary calcite minerals in the Class B fault zones remain enigmatic.

1. Introduction

Yucca Mountain Nevada (Fig. 1a), potential site of a high-level nuclear waste repository, is a ridge of Miocene (ca. 14 11.5 Ma) welded and non-welded pyroclastic flow and air fall tuffs of the Paintbrush Group, Calico Hills Formation and Crater Flat Group erupted from the Southwest Nevada Volcanic Field calderas (Sawyer et al., 1994). The mountain is part of the southern Great Basin of the central Basin and Range Physiographic Province (Fig. 1b). Yucca Mountain is an intra- basin horst within the Crater Flat Basin, a half-graben bounded on the west by the east-dipping Bare Mountain fault and on the east by a series of dominantly west-dipping faults that are antithetic to the Bare Mountain fault (Fig. 1c).

Within this framework, Yucca Mountain is a large, gently tilted fault block of Miocene tuffs, dipping approximately 5-10° to the east (Fig. 2a). It is bounded on the west by the Solitario Canyon fault and on the east by the Bow Ridge and Paintbrush Canyon faults (Fig. 2b). Most faults within the Yucca Mountain block are steeply dipping normal faults; however, oblique slip, strike-slip, high angle reverse, and low angle thrust faults are also present. Growth of the Paintbrush tuffs (ca. 12.8 - 11.45 Ma) across many of the faults, indicates that faulting initiated before or during tuff deposition (e.g., Day et al., 1998). Faulting activity is considered to be most significant in the Late Miocene between ca. 11 and 12 Ma (Fridrich et al., 1999), although faulting has remained active into the Holocene, as evidenced by historic seismicity (e.g., Rogers et al., 1991) and Quaternary faulting along most large faults at Yucca Mountain (e.g., Stepp, 2000).

The Nuclear Waste Policy Act of 1982 requires characterization of Yucca Mountain as a potential permanent repository to safely dispose of high-level radioactive waste for 10,000 years. The unprecedented long design life of the facility and the technical challenge of permanently disposing of high-level radioactive waste in a geologic repository, has prompted the Department of Energy to develop a 10.4 km long network of tunnels at a maximum depth of 300 meters beneath Yucca Mountain. The Exploratory Studies Facility (ESF) is a 7.6 m diameter, 7.8 km long tunnel from which the 6.1 m diameter, 2.6 km long Enhanced Characterization of the Repository Block (ECRB) tunnel was bored. Miocene volcanic tuffs of Yucca Mountain are of generally high strength and require minimal structural support,

allowing for nearly continuous three-dimensional exposures of rock.

Our analyses of faults and fault zones in the ESF and ECRB were initiated in 1998, mainly to refine models of faulting used in the Nuclear Regulatory Commission (NRC) repository performance assessment codes. Such models are essential to evaluate uncertainties in the risks associated with potential direct disruption of the emplaced waste by fault movements. Accurate models of faulting require a detailed description and understanding of faults at the repository horizon level. Results of our ESF/ECRB fault studies also bear on other components potentially affecting repository performance. In particular, our study has direct bearing on hydrologic models and conflicting interpretations of groundwater thermochronology at Yucca Mountain.

Our approach to gaining a better understanding of faulting was to examine in detail the fault rocks that comprise the fault zones. Fault-zone deformation in the upper crust produces a wide variety of morphologies indicative of the conditions and history of faulting. Idealized faults consist of two textural zones: a fault core and a damage zone (Sibson, 1977; Caine et al., 1996; Seront et al., 1998). The fault core is a zone of relatively high strain that typically accommodates most of the fault displacement by shear in gouge, cataclasite, breccia or mylonite. The surrounding damage zone is less deformed, accommodates less displacement, and may contain subsidiary structures such as joints, veins, and minor faults.

Deformation mechanisms govern the behavior of fault zones and their geometric and textural morphologies. At Yucca Mountain, the protolith (volcanic tuff) has undergone brittle deformation dominated by cataclasis at shallow levels in the upper crust. Changes in deformation mechanisms with time and increased fault displacement, the presence or absence of fluids in the fault zone, mineral transformations, and syndeformational mineralization affect the rheology of the fault zone, causing the active parts of the faults to widen or narrow with increasing displacement. Two-end member possibilities exist (Wojtal and Mitra, 1986): (1) Deformation produces fault rocks that inhibit further slip in the fault core, such that additional fault displacement causes the protolith to fracture and the fault zone to widen (thicken) with time (i.e., strain harden). (2) The fault rocks become progressively easier to deform such that deformation is localized to a narrow portion of the fault zone (i.e., strain localization or strain softening). In strain softening, the intensely deformed fault core incrementally accommodates more of the deformation, and there is no

further increase in fault- zone width. Investigations of faulting at Yucca Mountain, especially studies of faults exposed in the ESF, reveal that all these deformation processes and related features are present and subsets of faults with common morphology may be defined on the basis of this approach.

In this paper, we present results from detailed observations of fault zones exposed within Yucca Mountain. In particular, we present our findings of four different fault zone morphologies (Classes A, B, C, and D) and our interpretation of the genetic relationships between different fault types. The ramifications of these findings are then discussed in light of ongoing studies of secondary mineralization and paleohydrology at Yucca Mountain.

2. Faults in the ESF/ECRB

Our study examined faults at the ground surface, in trenches, in cores (VH2, USW-G1, and USW-G2) and in the ESF/ECRB. Our examination investigated the diversity of exposed fault expressions rather than a limited, spatially uniform approach sensitive to relative abundances of fault types. Most samples were vacuum impregnated with epoxy prior to thin section preparation. Samples were precisely oriented and cut along two mutually perpendicular directions. Transverse thin sections were cut normal to the fault plane and parallel to the dip direction of the fault. Longitudinal this sections were cut parallel to the strike of the fault and normal to the fault plane.

We prepared and examined 32 core, 32 surface and trench, and 117 ESF/ECRB thin sections. Thin sections from core samples provided useful contextual information but did not form the basis for any of our conclusions because those samples were only generally oriented, and larger scale fault architecture could not be deciphered from the cores alone. Samples from the surface and trench exposures are typically indurated with caliche, opal, and sepiolite (Hill et. al., 1995; Dublyansky et al., 1998; Stuckless et al., 1992). Mineralization dominates the fault rocks, making it difficult to determine the original fault rock fabrics or distinguish cemented surficial deposits from fault rock breccias. Some mineralization is clearly due to pedogenic surficial processes (e.g., root traces are present in some samples) although the total extent of pedogenic overprint is unclear and disputed (e.g., Hill et. al., 1995; Stuckless et al., 1998). ESF/ECRB

fault samples obviously do not contain any pedogenic overprint. For all of the reasons outlined above, this report is exclusively based upon the ESF/ECRB field observations, field data, and thin section analyses (Appendix 1).

Based on field studies and microstructural analyses, we recognize four broadly defined fault zone morphologies (Fig. 3). For ease of discussion we refer to these as Class A, B, C, and D fault zones, in order of increasing displacement. We recognize that displacement can vary with position along a single fault and that it is possible that fault zone architecture and therefore our classification of a given fault may be different if observed at the surface or in cores from deeper in Yucca Mountain. In general, fault zones at Yucca Mountain tend to widen as they approach the ground surface. For example, the Ghost Dance fault core is one meter wide in the ESF and is more than 10m wide 300m above at the surface. Displacement changes dramatically (1 to 30 m) along strike (Mongano et al., 1999). Narrow fault zones (< 1 m wide) and faults with displacements less than 3 m constitute the majority of the faults in Yucca Mountain (CRWMS/M&O, 1998; Fig. 4).

2.1 Class A

Class A faults have minor displacements of mm to a few cm. These faults have little to no fault core (less than 1 cm) and narrow damage zones (less than 2 cm; Fig. 5). The faults are best described as discrete sliding surfaces along which displacement has taken place by frictional sliding along well-defined fractures in the welded tuffs. Slickenlines are common. Secondary minerals such as chalcedony are present in thin films in the fault cores of some Class A faults. In those Class A faults that contain secondary minerals, the minerals do not appear to be offset by subsidiary fault displacements. The crystals do not show evidence of deformation, and the deposits simply fill in the relief formed by subsidiary fault offsets. Class A faults are abundant in the ESF.

Class A faults appear to have formed by brittle fracture of the protolith, frictional sliding, and propagation of subsidiary fractures and faults. Some Class A faults have narrow apertures into which secondary minerals have been precipitated. There is no indication that the secondary minerals were involved in the fault deformation and therefore, we interpret the minerals to be post-kinematic.

2.2. Class B

Class B faults have displacements of less than one meter with the notable exception of the Drill Hole Wash A fault splay (Appendix 1). Based on extrapolation from slickenline orientations and fault dip separation, the Drill Hole Wash A fault may have 14 m oblique net slip. Class B faults contain a well-developed fault core between 2 and 30 cm thick, averaging 7 cm in thickness (Fig. 6). Core thickness varies laterally and vertically both up and down dip. Thickness variations are most commonly associated with dilational jogs. The fault core boundaries are typically discrete, slickensided, and can contain multiple slickenline orientations. Class B faults have either poorly developed damage zones limited to a few cm wide or in some cases, no damage zone at all.

Fault cores consist of angular rock fragments and as much as 65% or more calcite matrix (Fig. 7a). The clasts are relatively intact and show little evidence of frictional attrition. Wall rock tuff fragments contain undisturbed eutaxitic foliation, indicating that no significant progressive cataclasis occurred prior to brecciation of the tuffs and entrainment in calcite. Tuff clasts are commonly angular and elongate creating tabular or rectangular shaped clasts (Fig. 7a). Despite the strong mechanical anisotropy created by the eutaxitic foliation (CRWMS M&O, 1997), the flat planar boundaries of the clasts are commonly at high angles to the eutaxitic foliation within the clasts (Fig. 8a and b). This angular relationship suggests that faulting initiated by closely spaced brittle fracturing sub-parallel to the fault zone boundaries. The dispersion of rock fragments is perhaps best described as a puzzle piece breccia. Some clasts can be graphically restored to fit into one another by simple rigid body translation and/or rotation. This fault rock texture requires significant dilation across the fault zones (beyond that needed during initial fault brecciation) but is not restricted to the dilational jogs commonly found in Class B faults.

Tuffaceous wall rock clasts are supported by calcite matrix with crystals ranging from coarse (e.g., 0.5 cm in diameter) to microcrystalline. Calcite deformation is dominated by abundant mechanical twins and intragranular fractures indicative of low temperature plasticity (Fig. 7a and b). Calcite strain gauge analysis of one Class B fault core indicates that deformation by mechanical twinning accumulated 2.24% extension (Gray et al., 1999). Calcite crystals are offset by less common intercrystalline fractures.

Intercrystalline shear fractures are confined to the crystalline matrix and do not crosscut wall rock clasts. Additional translational strain was accommodated by frictional sliding on the boundaries of the fault core as evidenced by well-developed slickenlines.

The matrix in many of the Class B fault rocks is poikilotopic, exhibiting large patches (mm scale) of crystallographically continuous calcite. Poikilotopic cements in sedimentary rocks are attributed to slow nucleation and growth rates (Folk, 1974; Tucker and Wright, 1990) and cement recrystallization (Friedman, 1965). The calcite matrix is not cathodoluminescent. The evidence from Class B faults suggests that fault displacement was principally accommodated by crystal-plastic deformation and intercrystalline frictional sliding of calcite since the earliest stages of fault movement. The wall rock clasts suspended in the calcite matrix underwent rigid body rotation during flow of the calcite matrix. Frictional sliding along the fault core/damage zone boundaries also accommodated some displacement. These deformation mechanisms are not conducive to strain hardening at the minor displacements associated with Class B faults. No large Class B faults with displacements and fault zone widths comparable to Class D faults exist in the ESF or ECRB.

Because the textural evidence supports rapid crystallization of a syn-kinematic calcite matrix, we interpret the poikilotopic texture to indicate recrystallization of the matrix. Since the poikilotopic calcite contains abundant deformation twins, the recrystallization was probably syn-kinematic as well. Class B fault cores also contain rare veins partially or entirely filled with relatively strain-free and inclusion free calcite (Fig.7c). These veins cut across the recrystallized, deformed core matrix and are therefore interpreted to be post-kinematic.

Initiation and development of the calcite textures in Class B faults is problematic. Wall rock inclusion trails indicative of a crack-seal mechanism of fracture dilation are not abundant. The matrix-supported crystalline breccia texture and dearth of crack seal textures suggests that initial crystallization of the calcite in Class B faults accompanied fault rupture and may have occurred rapidly. At shallow levels of burial and in an extensional environment, high pore fluid pressures during faulting are not likely. Alternatively, breccias may have formed by rapid decrease in pore fluid pressure causing implosion brecciation in dilational jogs (Sibson, 1986). Implosion breccias are known to have puzzle piece breccia textures; wall rock clasts have little internal deformation and are commonly matrix supported (Sibson, 1986; 1994; Seront et al., 1998).

In this interpretation, the calcite-saturated fluid would be integral to the faulting process and mineralization of the crystalline matrix would be syn-kinematic.

2.3 Class C

Class C faults have displacements of a few cm's to 10's of meters and have correspondingly well-developed fault cores ranging from 10's of cm to 1 m thick. Class C faults are from all slip classifications. One example of a Class C fault is the Ghost Dance Fault. It is interesting to note that all thrust faults found within the ESF/ECRB have Class C characteristics (Fig. 9). Minor faults typically bound fault cores. Damage zones range from 1 m to 10 m thick. Fault cores consist of non-cohesive to poorly cohesive, unfoliated cataclasite and breccia (Fig. 10a). Fault cores contain antithetic and synthetic faults that connect floor to roof of the cores or tie into other minor faults, giving a macroscopic appearance of slickensided blocks of cataclasite/gouge within the fault core. In thin section, fault core is composed of cataclasite bounded by discrete intergrangular sliding surfaces. The cataclasite is composed of tuffaceous wall rock fragments and clasts of cataclasite ranging from several cm in diameter to sub-microscopic. Tuff fragments are angular to sub-rounded and slightly elongate to equant. The modal orientation of the long dimension of the clasts is sub-parallel to the eutaxitic foliation (Fig. 8c). Fractures that bound clasts exhibit a wide variety of orientations relative to the primary foliation in the clasts (Fig. 8d). When compared to the Class B fault clasts, Class C fault clasts appear to have a higher proportion of clast bounding fractures sub-parallel to the primary foliation (Fig. 8b and d). Secondary mineralization in Class C faults is rare. Small chalcedony veins are offset by intergranular shears (Fig 10b).

Class C faults appear to have formed by cataclasis and frictional sliding in the fault core. Progressive clast size reduction occurred by brittle fracture of clasts, preferentially sub-parallel to the eutaxitic foliation, and by transgranular sliding between packets of cataclasite.

2.4 Class D

Class D faults have 10 m to 100's m displacements. These faults have meters-wide fault cores and

broad damage zones tens of meters wide. Examples of Class D faults are the Solitario Canyon Fault (~300 m dip separation, Mongano et al., 1999) and the Dune Wash Fault (52 m dip separation, Eatman et al., 1997). Fault cores are composed primarily of poorly cohesive breccia with a cohesive, foliated gouge at or near the center of the core (Fig. 11). X-ray diffraction analyses confirm that the Solitario Canyon fault gouge consists of smectite (Appendix 2; Fig. 12), possibly the product of translocated altered tuffs (Levy, 1999). This gouge is 2 to > 8 cm thick and contains a composite foliation (Fig.13). The foliation is reminiscent of C-S structure in mylonites or P & R structure of Cladouhos (1999). One foliation lies parallel to the gouge boundary and one lies at 40° and is synthetic to the main shear direction. Gouge in the Dune Wash Fault has three foliations: one fault parallel set of shears, one very prominent phyllosillicate preferred orientation foliation at 30° to the fault (dihedral angle opens in the direction of shear, "P-foliation", after Cladouhos, 1999) and a more widely spaced, well developed synthetic foliation at 20° to the fault (Riedel shear or R-foliation, Cladouhos, 1999). The P-foliation is asymptotic into the Riedel shears and fault-parallel shears. The foliations wrap around survivor grains and exhibit both δ and σ type tails indicating that clasts underwent rotations during shear of the gouge. Some cooling joints elsewhere in the ESF/ECRB have 2-4 cm thick fillings of translocated swelling clays. These cooling joints have been reactivated and undergone minor amounts of displacement (Sweetkind and Williams-Stroud, 1996). The clays are organized in a similar fashion to Class D gouge, containing a well-developed P-foliation, suggesting that large displacements are not required to develop a P- foliation in the clay-rich fracture fill. The breccia surrounding the gouge varies from being partially mineralized with silica phases and calcite to being unmineralized. The breccia clasts are composed of comminuted fault rock and may be enveloped by slickensided surfaces. Field and microstructural relationships suggest that Class D faults underwent cataclastic flow in the fault core and brittle fracture accompanied by some polymineralic secondary mineralization in the damage zone.

3. Genetic relationships between faults

Classes A, C, and D may be genetically linked, having experienced progressive grain size reduction with increased fault displacement. Class A faults accommodated deformation by brittle fracturing and

cataclastic flow. As grain size was reduced with increased displacement, the fault core underwent strain hardening, and the fault zone widened to form a Class C fault zone morphology. Further displacement, such as that associated with Class D faults, may have promoted alteration of volcanic rocks to smectite and translocation of clays in part of the fault core. The smectite weakened the fault core, localizing most of the subsequent displacement to a narrow zone of foliated gouge. Although cataclastic flow in Class A, C, and D faults may intrinsically require some small component of fault-normal dilation due to rigid body rotation of tuff fragments in the fault core and disorganization of the rock due to cataclasis, we do not consider these faults to be significantly dilational. There is no evidence to indicate that these rocks underwent a significant volume change during faulting.

Class B faults appear to have distinctive orientations when compared to the general population of faults in the ESF/ECRB (Fig. 14a and 14b). Class B faults generally strike NW-SE and contain a variety of slickenline orientations, among which low and high rake slickenlines are most common. One fault rock sample contains two slickenline orientations (one oblique and one horizontal). The oblique slickenlines originate from ridges formed by the strike-parallel set indicating that the strike parallel set predates and localized the formation of the younger, oblique set. A calcite strain gauge analysis of the same Class B fault rock indicates a right lateral strike slip history for a Class B fault at ESF station 43+39 (Fig. 15) but does not reflect oblique-slip deformation. Apparently, the younger, oblique-slip event did not involve crystal plastic deformation of calcite in the fault core.

4. Implications for paleohydrology and present day hydrology at Yucca Mountain

4.1 Origin and timing of calcite mineralization in Class B faults

Yucca Mountain consists of siliceous volcanics, therefore calcite mineralization must be explained by movement of calcium carbonate rich waters into the tuffs from elsewhere. The ESF/ECRB (and the proposed repository horizon) currently lie within the vadose zone, 300 m above the water table. Paces et al. (1998) contend that the repository horizon has been within the vadose zone since deposition of the tuffs. They point out that most lithophysal cavities are unfilled or only partially filled with secondary minerals and

that mineralization is generally restricted to the floors of the cavities. Those lithophysal cavities that contain secondary minerals typically contain both opal and calcite as well as less common fluorite, quartz, and chalcedony. Studies of mineral paragenesis in lithophysal cavities have led to development of a model of sequential mineralization, beginning during deposition of the tuffs and extending to the Quaternary. Paces et al. (1996) found that the lithophysae yield the most complete record of this history and that fractures (including faults) typically only record a partial history. Paces et al. (1998) recognized early, middle, and late stages of mineralization with overlapping but on average, different C and O isotopic signatures (Figure 16). Calcite is found at all major stages of deposition (Paces et al., 1996; Cline and Wilson, 2001). Neymark and Paces (2000) developed a steady, continuous growth model for mineralization in a vadose environment. They estimate that secondary minerals were deposited at a constant rate of less than 5 mm/m.y. Sr, O, and C isotopic signatures have been interpreted to indicate that the source of calcium carbonate was meteoric water from above throughout the post-depositional history of the tuffs (Paces et al., 1998; Whelan and Moscati, 1998). Dublansky et al. (2001) pointed out that two-phase fluid inclusion assemblages, some containing evidence of hydrocarbons, are present in calcite. Wilson et al. (2001) conducted a comprehensive fluid inclusion microthermometry study on samples collected in the ESF/ECRB. They confirmed average homogenization temperatures for two-phase fluid inclusion assemblages of about 50-60 °C. This and an alternative explanation for the isotopic signatures of the secondary minerals has led Dublyansky et al. (2001) to conclude that at least some of the secondary minerals found in lithophysal cavities were precipitated from water with elevated temperature derived from below Yucca Mountain. They suggest that warm water invaded the repository horizon several times in the past and potentially in the recent past. Our results bear on this issue.

4.1.1 Textures

Growth textures indicative of vadose zone conditions (e.g., pendant growth, gravity asymmetry, onlapping, and meniscus) are found in the secondary mineral crust on the floors of lithophysal cavities (Paces et al., 1998; Cline and Wilson, 2001). In contrast, Class B faults have no textures indicative of vadose zone saturation. Rather, they have sparry, mosaic, or isopachous calcite matrix, and partially filled, post-kinematic calcite veins that transect fault cores exhibit void-filling, drusy textures. These textures are

indicative of saturated conditions during mineralization.

4.1.2 Paleotemperatures

Although we have identified two-phase fluid inclusion assemblages in the sparry calcite from Class B faults, we chose not to collect fluid inclusion microthermometry data. Calcite fluid inclusion microthermometry is not well suited to fault rocks because calcite deforms readily by crystal plasticity and is subject to diffusion related deformation mechanisms at low temperatures. These deformation mechanisms may cause volume changes, distortions, and chemical changes to the fluid inclusions, ultimately compromising the microthermometry data.

Experimental and field based studies demonstrate that the thickness of mechanical twins (sometimes referred to as "deformation twins") in calcite correlates with the temperature at which calcite deformed (Ferrill, 1991, 1998; Burkhard, 1993). Mechanical twins wider than 1 μ are considered "thick" and require elevated temperatures of deformation. Deformation twins from calcite in a Class B fault examined on a universal stage were determined to have an average mechanical twin width of 1.43 μ (Gray et al., 1999). The mechanical twins are curved and taper laterally. This average twin width and morphology requires natural temperatures in excess of 150 °C (Ferrill, 1991, 1998; Burkhard, 1993).

4.1.3 Chemsitry

Systematic decreases of δ 13CPDB from about +10 to 10 per mil. and increases in δ18OSMOW from about +10 to +21 per mil. with decreasing relative mineral age from calcite in lithophysae and fractures are interpreted to be an artifact of a meteoric source responding to climate change (Paces et al., 1996; Whelan and Moscati, 1998). Isotopic data from one Class B fault (ESF Sta 76+17) exhibits δ 13CPDB values ranging from +2.5 to 7 per mil. and δ18OSMOW ranging from about +14 to +18.5 per mil (J. Whelan, 2000, personal communication; Fig. 16). These values are similar to those of intermediate and late stage secondary calcite from the ESF/ECRB (Paces et al., 1998).

4.1.4 Origin

The mineralization in Class B faults is distinctive when compared to other occurrences in Yucca

Mountain. Lithophysal cavities contain diverse crystal forms of calcite and other minerals that have been interpreted to record an extensive and protracted history of characteristically polymineralic secondary mineralization (e.g., Paces et. al., 1996; Neymark and Paces, 2000). Paces et al. (1996) and Cline and Wilson (2001) interpret the lithophysal cavities to record vadose conditions. Fluid inclusion microthermometry in calcite from lithophysae and partially filled fractures yields homogenization temperatures not greater than 81 °C (Wilson et al., 2001) to 85 °C (Dublyansky et al., 2001). Because the Micocene tuffs of Yucca Mountain were never deeply buried, the homogenization temperatures are interpreted to represent trapping temperatures (Dublyansky et al., 2001; Wilson et al., 2001).

In contrast, Class B faults contain textures indicative of water-saturated conditions. Class B faults have sparry calcite with poikilotopic texture suggestive of recrystallization. The sparry calcite contains mechanical twins indicative of deformation at temperatures in excess of 150 °C. The sharp difference between calcite mineralization in Class B faults compared to the mineralization in lithophysal cavities leads us to conclude that the thermal and hydrologic history of Yucca Mountain was complex and that the origin of the secondary minerals was polygenetic. Thermal-hydrologic mechanisms that can explain this complex and polygenetic mineral history remain elusive. If we assume that the Class B faults formed shortly after caldera eruptions and deposition of the tuffs (11- 13 Ma), then fault-related mineralization observed in Class B faults could be explained by circulating hot fluids related to contemporaneous volcanic-geothermal activity. However, the C and O isotopic ratios in the one Class B fault analyzed (Fig. 16) are inconsistent with this interpretation. Calcite in the Class B faults has C and O isotopic signatures similar to intermediate and late stage calcite in the lithophysal cavities.

Conversely, if we assume that the Class B faults formed more recently, well after the tuffs cooled, then the C and O isotopic ratios are compatible with the long-term evolution of those isotopes as proposed by Paces et al. (1998). Nevertheless, the elevated 150 °C temperatures indicated by the thick mechanical twins would thus require an episode of tectonic-thermal activity at Yucca Mountain well after the tuffs cooled ca. 10 Ma. Although seismically-activated episodes have been proposed to explain secondary mineralization and fluid inclusion temperatures up to 85 °C (e.g., Dublyansky et al., 2001), their occurrence is highly controversial (c.f., Dublyansky et al., 2001 with Paces et al., 1998). Geologic evidence of hydrothermal activity at Yucca Mountain within the past 10 Ma sufficient to develop the Class B faults with

calcite-twin deformation temperatures above 150 °C is, at best, equivocal (cf. Dublyansky, 2001 with Wilson et al., 2001).

Unfortunately, the age of class B faults, absolute or relative to other faults or secondary minerals in lithophysal cavities, is unknown. We observed a very limited set of cross-cutting relationships in the ESF/ECRB (Appendix 1, Table 1). Of the five cross-cutting relationships noted, only three suggest that NW-trending faults (such as the majority of class B faults) predate N-S or NE trending faults. This lack of age control (relative or absolute) on Class B faults limits our ability to interpret their origin within existing thermal-hydrology models of Yucca Mountain. As recognized by the National Academy of Sciences (NAS,1992), adequate and reliable age control is essential to resolution of the paleothermal debate at Yucca Mountain.

4.2 Faults as Fluid Barriers or Conduits

A primary control on the permeability architecture of stratified rocks is the difference in permeability of sequential rock layers. If the stratigraphic sequence is undeformed, the vertical heterogeneity and anisotropy will dominate the permeability architecture. However, ground water temperature variations (Brikowski, 1997) and hydraulic head differences in the deep aquifer beneath Yucca Mountain (Bredehoeft, 1997) indicate that faults significantly affect the present-day hydrology of Yucca Mountain. Faulted aquifers such as those at Yucca Mountain are influenced by aquifer communication between fault blocks (Allan, 1989), fault rock fluid barriers and pathways (Caine et al., 1996; Bredehoeft, 1997; Seront et al., 1998), permeability anisotropy due to minor fault arrays (Ferrill et al., 2000), and enhanced permeability due to dilation of faults responding to contemporary stress (Finkbeiner et al., 1997; Ferrill et al., 1999; Ofoegbu et al., 2001).

The precise architecture of a fault zone may have a significant impact on permeability (Evans et al., 1997). Fault cores may have lower permeability than the protolith because they can form by grain size reduction, primary porosity reduction, mineral transformations, and secondary mineralization. At shallow levels of the crust, the gouge or cataclasite therefore is expected to have relatively low permeability and may effectively form a barrier to fluid flow (Goddard and Evans, 1995; Caine et. al., 1996). In contrast,

damage zones may have enhanced permeability due to fracturing and subsidiary faulting (Evans et al., 1997). Coarse grained, unmineralized fault cores and/or damage zones consisting of open fractures may have greater permeability than the protolith, behaving as fluid conduits (Chester and Logan, 1987).

Our four classes of fault architecture can be placed within a hydrologic classification scheme devised by Caine et al. (1996). Class A faults, with their discrete sliding surfaces and narrow damage zones may be localized conduits. Class B faults have well developed mineralized cores and negligible damages zones. The high aspect ratios of wall rock clasts, late stage, low strain calcite filled veins sub-parallel to the fault zone boundaries, and the volume of calcite matrix in Class B fault breccias indicate that these narrow fault zones underwent significant dilation during faulting. Textures suggestive of saturated conditions within the fault core indicate that Class B faults were fluid conduits when they formed. Fluids may have assisted the faulting process by initiating fault rupture and subsidiary fracture propagation by hydraulic means. The fault rock textures are consistent with implosion breccia documented elsewhere (e.g., Sibson, 1994; Seront et al., 1998). Once crystallized, the calcite served to weaken the fault rock as the calcite underwent mechanical twinning and fracturing. These faults may now serve as localized barriers to fault-normal flow because they are so heavily mineralized (Seront et al., 1998). Class C faults have intensely fractured damage zones and cores consisting of unfoliated cataclasite and gouge. These may constitute a distributed conduit for fluid flow both across and along the faults. Class D faults are the most complex. Their well-developed damage zone surrounding a foliated gouge core produces a combined conduit- barrier system. Bulk anisotropy in fault zone permeability arises as fault-parallel flow is focused in the damage zone between the clay-rich core and relatively intact welded tuff protolith (Evans et al., 1997).

The temporal development of these hydrologic components can be incorporated into paleohydrologic models. Class B fault barriers are not likely to have had a large impact on the hydrology of Yucca Mountain after they formed, because they appear to represent a minor population of faults, and they are not likely to have large fault areas given their minor average displacements. Classes A and C faults developed sequentially and as hydrologic components, they would cause increased fault-parallel permeability with increased fault-related strain. Major block bounding faults (Class D) developed into combined conduit-barrier systems acting to impede aquifer communication between blocks and enhance fault-parallel flow. Because each class of faults has a characteristic range of fault widths and different internal

architecture, hydrologic models that incorporate faults should be sensitive to both fault width and corresponding likely hydrologic characteristics associated with those widths. Furthermore, the hydrologic properties of major block bounding faults are likely to change with displacement variations up and down dip and laterally. The clay-rich core of Class D faults is likely to give way to the distributed conduit characteristics of Class C faults near the fault tip.

5. Conclusions

Detailed examination of faults in the ESF and ECRB of Yucca Mountain reveal four fault classes. Three of these fault classes (Class A, C, and D) represent a continuum of fault deformation related to increasing displacement and associated mechanical response of the tuffaceous rocks. Faulting initiated along joints or fractures as discrete shears (Class A), followed by progressive cataclasis (Class C) eventually leading to the development of a foliated gouge core and intensely fractured damage zone (Class D).

The fourth class of faults at Yucca Mountain (Class B) represents an unusual faulting style in which faults of generally minor displacement are heavily mineralized with blocky calcite during fault initiation. Continued displacement after fault rupture was accommodated by crystal plastic deformation and intra/inter crystalline fracture and sliding of the calcite, and by discrete sliding along the core/damage zone boundaries. Class B faults are particularly significant because they constitute a secondary mineral occurrence that appears to be distinctly different from those found in lithophysae and fractures. In particular, they contain textures indicative of calcite mineralization in a fluid-saturated environment and deformation at elevated (>150 °C) temperatures. The age and origin of the Class B faults is unknown. Morphology and textures suggest that the Class B faults may be related to deformation of the tuff strata at Yucca Mountain soon after the tuffs were deposited 11-12 Ma. The chemical signature of the Class B faults, however, is similar to intermediate to late stage secondary minerals, suggesting that the faults may have formed later in the thermal-tectonic development of Yucca Mountain. At present this lack of age control (relative or absolute) limits our ability to interpret their origin within existing tectonic-thermal models.

The diversity of fault zone morphologies found in Yucca Mountain is important to paleohydrology and present-day hydrologic properties of Yucca Mountain. Class D block- bounding faults have fault zone

architecture that is conducive to fault parallel flow and impedes fault-normal flow. The hydrologic properties of smaller displacement faults within blocks should not be over generalized. Three distinct morphologies exist with different hydrologic properties ranging from discrete (Class A) to distributed (Class C) conduits and localized barriers (Class B).

Acknowledgements

We thank Alan Morris and Patrick Mackin for providing helpful comments on this manuscript and Deborah Waiting for assistance with figure preparation. The work was supported by the U.S. NRC (Contract NRC 02-97-009). This work is an independent product of the CNWRA and does not necessarily reflect the views or regulatory position of the NRC.

References

Allan, U.S., 1989. Model for hydrocarbon migration and entrapment within faulted structures. American Association of Petroleum Geologists Bulletin 73, 803-811.

Bredehoeft, J.D., 1997. Fault permeability near Yucca Mountain. Water Resources Research 33, 2459-2463.

Brikowski, T., 1997. Fault-controlled vertical leakage inferred from water-table temperature variations at Yucca Mountain. Nuclear Waste Projects Office Technical Report 025-97, State of Nevada Agency for Nuclear Projects.

Burkhard, M., 1993. Calcite twins, their geometry, appearance and significance as stress- strain markers and indicators of tectonic regime; a review. Journal of Structural Geology 15, 351-368.

Caine, J.S., Evans, J.P., Forester, C.B., 1996. Fault zone architecture and permeability structure. Geology 24, 1025-1028.

Chester F.M., Logan, J.M.,1987. Composite planar fabric of gouge from the Punchbowl Fault, California. Journal of Structural Geology 9, 621-634.

Cladouhos, T.T., 1999. A kinematic model for deformation within brittle shear zones. Journal of Structural Geology 21, 437-448.

Cline, J.S., Wilson, N.S.F. 2001. Paragenesis of secondary mineralization at Yucca Mountain, Nevada, U.S.A. In: Cidu, R. (Ed.), Water-Rock Interaction 2001. Proceedings of the Tenth International Symposium on Water-Rock Interaction, Balkema, The Netherlands, pp. 1311-1314.

CRWMS M&O (Civilian Radioactive Waste Management System Management and Operating Contractor), 1997. Yucca Mountain site geotechnical report. B00000000-01717- 5705-00043 REV 01. Las Vegas, Nevada: CRWMS M&O.

CRWMS M&O (Civilian Radioactive Waste Management System Management and Operating Contractor), 1998. Geology of the Exploratory Studies Facility Topopah Spring Loop. BAB000000-01717-0200-00002, REV01. U.S. Department of Energy, Las Vegas, Nevada.

Day, W.C., Dickerson, R.P., Potter, C.J., Sweetkind, D.S., San Juan, C.A., Drake, R.M., II, Fridrich, C.J.,1998. Bedrock geologic map of the Yucca Mountain area, Nye County, Nevada. U.S. Geological Survey Map I-2627, scale 1 : 24,000.

Dublyansky, Y., Ford, D., Reutski, V., 2001. Traces of epigenetic hydrothermal activity at Yucca Mountain, Nevada; preliminary data on the fluid inclusion and stable isotope evidence. Chemical Geology 173, 125-149.

Dublyansky, Y., Szymanski, J., Chepizhko, A., Lapin, B., Reutski, V., 1998. Geological history of Yucca Mountain (Nevada) and the problem of a high-level nuclear waste repository. In: Stenhouse, M.J., Kirko, V.I. (Eds.), Defence Nuclear Waste Disposal in Russia. NATO Series Kluwer Academic Publishing, Netherlands, pp. 279-292.

Eatman, G.L.W., Singleton, W.L., Moyer, T.C., Barr, D.L., Albin, A.L., Lung, R.C., Beason, S.C., 1997. Geology of the south ramp Station 55+00 to 78+77, Exploratory Studies Facility, Yucca Mountain Project, Yucca Mountain, Nevada. Department of Energy Report, DTN GS96090831224.020.

Evans, J.P., Forester, C.B., Goddard, J.V., 1997. Permeability of fault-related rocks, and implications for hydraulic structure of fault zones. Journal of Structural Geology 19, 1393-1404.

Ferrill, D.A., Morris, A.P., Stamatakos, J.S., Sims, D.W, 2000. Crossing conjugate normal faults. American Association of Petroleum Geologists Bulletin 84, 1543-1559.

Ferrill, D.A., 1991. Calcite twin widths and intensities as metamorphic indicators in natural low-temperature deformation of limestone. Journal of Structural Geology 13, 667-675.

Ferrill, D.A., Winterle, J., Wittmeyer, G., Sims, D.W., Colton, S., Armstrong, A., Morris, A.P., 1999. Stressed rock strains groundwater at Yucca Mountain, Nevada. Geological Society of America Today 9, 1-8.

Ferrill, D.A., 1998. Critical re-evaluation of differential stress estimates from calcite twins in coarse-grained limestone. Tectonophysics 285, 77-86.

Finkbeiner,T., Barton, C.A., Zoback, M.D., 1997. Relationships among in-situ stress, fractures and faults, and fluid flow: Monterey Formation, Santa Maria basin, California. American Association of Petroleum Geologists Bulletin 81, 1975-1999.

Folk, R.L., 1974. The natural history of crystalline calcium carbonate: Effect of magnesium content and salinity. Journal of Sedimentary Petrology 44, 40-53.

Fridrich, C.J., Whitney, J.W., Hudson, M.R., Crowe, B.M., 1999. Late Cenozoic extension, vertical axis rotation, and volcanism in Crater Flat basin, southwest Nevada. In: Wright, L., Troxel, B. (Eds.), Cenozoic Basins of the Death Valley Region. Geological Society of America Special Paper 333, pp. 197-212.

Friedman, G.M., 1965. Terminology of crystallization textures and fabrics in sedimentary rocks. Journal of Sedimentary Petrology 35, 643-655.

Frizzell, V.A., Schulters, J., 1990. Geologic map of the Nevada Test Site, southern Nevada. U.S. Geological Survey Map I-2046, scale 1:100,000.

Goddard, J.V., Evans, J.P., 1995. Fluid-rock interactions in faults of crystalline thrust sheets, northwestern Wyoming, U.S.A. Inferences from geochemistry of fault-related rocks. Journal of Structural Geology 17, 533-549.

Gray, M.B., Stamatakos, J.A., Ferrill, D.A., Evans, M.,A. 1999. Fault behavior and fault zone architecture in Miocence tuffs at Yucca Mountain. EOS, Transactions of the American Geophysical Union 80 (46), 741.

Hill, C. A., Dublyansky, Y.V., Harmon, R.S., Schluter, C.M.,1995. Overview of calcite/opal deposits at or near the proposed high-level nuclear waste site, Yucca Mountain, Nevada, USA; pedogenic, hypogene, or both? Environmental Geology 26, 69-88.

Levy, S., Chippera, S.,WoldeGabriel, G, Fabryka-Martin, J., Roach, J., Sweetkind, D.S., 1999.

Flow-path textures and mineralogy in tuffs of the unsaturated zone. In: Haneberg, W.C., Mozley, P.S., Moore, J.C., Goodwin, L.B. (Eds.), Faults and Subsurface Fluid Flow in the Shallow Crust. Geophysical Monograph 113, pp.159- 184.

Mongano, G.S., Singleton, W.L., Moyer, T.C., Beason, S.C., Eatman, G.L.W., Algin, A.L., Lung, R.C., 1999. Geology of the ECRB Cross Drift Exploratory Studies Facility, Yucca Mountain Project, Yucca Mountain, Nevada. http://www.ymp.gov/timeline/site/spg2gm3_a/

Moore, D.M., Reynolds, R.C., 1989. X-ray diffraction and the identification and analysis of clay minerals. Oxford University Press, Oxford.

NAS (1992) Ground water at Yucca Mountain - How high can it rise? Final Report of the Panel on Coupled Hydrologic/Tectonic/Hydrothermal Systems at Yucca Mountain.

National Academy Press, Washington, D.C. Neymark, L.A., Paces, J.B., 2000. Consequences of slow growth for 230Th/U dating of Quaternary opals, Yucca Mountain, NV, USA. Chemical Geology 164, 143-160.

Ofoegbu, G.I., Painter, S., Chen, R., Fedors, R.W., Ferrill, D.A., 2001. Geomechanical and thermal effects on moisture flow at the proposed Yucca Mountain nuclear waste repository. Nuclear Technology 134, 241-262.

Paces, J. B., Marshall, B.D., Whelan, J.F., Neymark, L.A., Peterman, Z.E., 1998. Summary of calcite and opal deposits in the Exploratory Studies Facility and estimates of the distribution and isotopic compositions of these minerals along the east-west cross drift alignment, Yucca Mountain, Nevada: U.S., Geological Survey Open-File Report.

Paces, J. B., Neymark, L.A., Marshall, B.D., Whelan, J.F., 1996. Ages and origins of subsurface secondary minerals in the Exploratory Studies Facility (ESF). U.S. Geological Survey Yucca Mountain Project Branch 1996 Milestone Report 3GQH450M, Denver CO. U.S. Geological Survey.

Rogers, A.M., Harmsen, S.C., Corbett, E.J., Priestly, K., DePolo, D., 1991. The seismicity of Nevada and some adjacent parts of the Great Basin. In: Slemmons, D.B., Engdahl, E.R., Zoback, M.D., Blackwell, D.D. (Eds.), Neotectonics of North America. Geological Society of America, Denver, CO, pp. 153-184.

Sawyer, D.A., Fleck, R.J., Lanphere, M.A., Warren, R.G., Broxton, D.E., Hudson, M.R., 1994. Episodic caldera volcanism in the Miocene southwestern Nevada volcanic field: revised stratigraphic framework, 40Ar/39Ar geochronology, and implications for magmatism and extension. Geological Society of America Bulletin 106, 304-1318.

Seront, B., Wong, T.-F.., Caine, J.S., Forster, C.B., Bruhn, R.H., Fridrich, J.T., 1998. Laboratory characterization of hydromechanical properties of a seismogenic normal fault system. Journal of Structural Geology 20, 865-881.

Sibson, R.H., 1977. Fault rocks and fault mechanisms. Journal of the Geological Society 133, 191-213.

Sibson, R. H., 1986. Brecciation processes in fault zones: Inferences from earthquake rupturing. Pure and Applied Geophysics 124, 159-175.

Sibson, R. H., 1994. Crustal stress, faulting and fluid flow. In: Parnell, J. (Ed.), Geofluids: Origin, Migration, and Evolution of fluids in Sedimentary Basins. Geological Society Special Publication 78, pp. 69-84.

Starkey, H.C., Blackmon, P.D., Hauff, P.L., 1984. The routine mineralogical analysis of clay-bearing samples. U.S. Geological Survey Bulletin B 1563.

Stepp, J.C., Wong, I., Whitney, J., Quittmeyer, R., Abrahamson, N., Toro, G, Youngs, R., Coppersmith, K., Savy, J., Sullivan, T., Yucca Mountain PSHA Project Members, 2000. Probabilistic Seismic Hazard Analyses for Ground Motions and Fault Displacements at Yucca Mountain, Nevada. Earthquake Spectra17,13 151.

Stuckless, J.S., Marshall, B.D., Vaniman, D.T., Dudley, W.W, Peterman, Z.E., Paces, J.B., Whelan, J.F., Taylor, E.M., Forester, R.M., O'Leary, D.W., 1998. Overview of calcite/opal deposits at or near to the proposed high-level nuclear waste site, Yucca Mountain, Nevada, U.S.A.: Pedogenic, hypogene, or both?; discussion. Environmental Geology 34, 70-78.

Stuckless, J.S., Peterman, Z.E., Forester, R.M., Whelan, J.F., Vaniman, D.T., Marshall, B.D., Taylor, E.M., 1992. Characterization of fault-filling deposits in the vicinity of Yucca Mountain, Nevada. Waste Management 1992 Conference Proceedings, Tucson, AZ Waste Management, 929-935.

Sweetkind, D.S., Williams-Stroud, S.C., 1996. Characteristics of fractures at Yucca Mountain, Nevada: Synthesis report. U. S. Geologic Survey Administrative Report, Denver Co. U.S. Geological Survey.

Tucker, M.E., Wright, V.P., 1990. Carbonate Sedimentology. Blackwell Scientific Publications, Oxford.

Whelan, J.F., Moscati, R. J., 1998. 9 M.Y. record of Southern Nevada climate from Yucca Mountain secondary minerals. Proceedings of the Eighth International Conference on High Level Radioactive Waste Management, pp. 12-15.

Wilson, N.S.F., Cline, J.S., Amelin, Y., 2001. Temporal constraints for elevated temperature fluids at the potential Yucca Mountain nuclear waste repository, U.S.A. In: Cidu, R. (Ed.), Water-Rock Interaction 2001. Proceedings of the Tenth International Symposium on Water-Rock Interaction, Balkema, The Netherlands, 1407-1410.

Wojtal, S.F., Mitra, G., 1986. Strain hardening and strain softening in fault zones from foreland thrusts. Geological Society of America Bulletin 97, 674-687.

Appendix 1.

Structural data collected by the authors listed ESF/ECRB are listed in Table 1. Consolidated sample numbers correspond with those assigned by the Sample Management Facility at the Nevada Test Site. Lithostratigraphic units and thermal/mechanical units are from Mongano et al. (1999). 36Cl/Cl data are from Levy et al.(1999).

Appendix 2.

This appendix constitutes documentation of a clay mineralogy investigation on Solitario Canyon Fault gouge specimen SPC00543707 collected at ECRB Station 25+85.1. Sample analyses were performed on a Philips Automated Powder Diffractometer, housed in a climate and humidity controlled room and maintained by the Department of Geology at Bucknell University. The diffractometer is supported by an XRG - 3000 generator, an APD - 3720 computer control cabinet, a PW 1710 diffractometer control unit and a copper long fine focus tube. An IBM Pentium PC is interfaced with the diffractometer and has two Philips software support packages: PC APD, ver. 3.6 (control software) and PC identify, ver. 1.0f (search-match software). The diffractometer undergoes semi-annual maintenance inspections performed by Philips technicians under a service contract with the Department of Geology at Bucknell University. A 400-mesh quartz standard sample mounted on a low-background holder is used as a control. If the standard produces a diffraction pattern that deviates from the expected pattern, the machine is recalibrated. The calibration of the machine was checked in this way immediately before the Solitario Canyon Fault samples were analyzed. The x-ray diffractometer required no adjustment.

Analytical Procedures

Three different analyses were performed on sample remnants. X-ray diffraction patterns were generated from one random powder mount and two oriented powder mounts. One oriented powder mount was air-dried, and the other was treated with ethylene glycol following the procedures of Moore and Reynolds (1989).

Procedure for sample preparation of random powder mount

1. Sample fragment was crushed and dry sieved.
2. The fraction that passed through the 400 mesh sieve was placed inside a back-loaded sample holder

and inserted into the x-ray diffractometer to be analyzed. The resulting x-ray diffraction pattern included a peak at 6.13° 2θ (14.42Å d-spacing), indicating the presence of certain clay groups.

Procedure for sample preparation of oriented powder mounts

1. Approximately 20 g of sample was gently crushed and placed in a clean beaker with 200 ml of distilled water.
2. Approximately 0.25 g of sodium hexametaphosphate was added to the suspension.
3. The beaker containing the mixture was then placed in an ultrasonic bath at room temperature for approximately 10 minutes to encourage disaggregation.
4. The mixture was poured into a 1000 ml graduated cylinder.
5. Distilled water was added to the mixture until the total volume of the mixture was raised to 1000 ml.
6. The mixture was then stirred.
7. The mixture was then left undisturbed for 3 hours and 50 minutes.
8. A pipette was used to draw off the uppermost 5 cm of the mixture. The extracted suspension should have contained suspended particles of 2diameter or less.
9. Three oriented powder mounts were prepared using the Millipore Filter Transfer Method detailed in Moore and Reynolds (1989).

Procedure for air-drying of two oriented powder mounts

1. The oriented powder mounts were allowed to air dry at room temperature. As this occurred, the mount was observed to curl at the edges. The result is x-ray diffraction pattern 543707O.DI. A broad peak at 6.07° 2θ (probably the result of curling) corresponds to a 14.55 Å d-spacing peak.

Procedure for glycolating oriented powder mount

1. One oriented powder mount was exposed to ethylene glycol vapors at 60 °C for 4 hrs. in a closed

container.

2. The powder mount was extracted and immediately placed in the x-ray diffractometer and analyzed. The mount did not curl. The resulting x-ray diffraction pattern was labeled 543707G.DI. A peak at 16.6Å d-spacing indicates a shift characteristic of smectites (Starkey and others, 1984).

Table 1. Fault and Related Feature Data.

Locality	Sample identification number	Lithostratigraphic unit Mongano et al., 1999	thermal/ mech unit Mongano et al., 1999	Fault Class	Orientation strike, dip angle & dip direction	Slickenlines trend, plunge	Separation	Core width	Notes	Cl-36/Cl data Levy et al., 1999; bold = anomalous	Figure
ESF 28+81.5	SPC00566356, SPC00566355, SPC00566354	ppopah - Tptpm	Tsw2	A	153, 40N			3mm, 20 cm max	field photos		
ESF 35+92.5	none	ppopah - Tptpm	Tsw2	A					050, 90 strike slip fault terminates against Sundance.		
ECRB 13+06	SPC00566358	ppopah - Tptpm	Tsw2	A	285, 83N	284, 10		1 mm	shear		
ESF 15+66	SPC00566371	Topopah - Tptrn	TSw1	B	176, 69W		reverse dip separation				
ESF 16+19.2	SPC00566368	Topopah - Tptrn	TSw1	B	145, 87E		normal dip separation			982; "fracture"	
ESF 19+36.5	SPC00566362, SPC00566363	opopah - Tptpu	TSw1	B	300, 85S	299,09		25cm, 30 cm max	Drill Hole Wash A; field		
ESF 27+65	SPC00566357	ppopah - Tptpm	Tsw2	B	322, 38N	346,17		11.5 cm, 20 cm max			
ESF 32+23.5	SPC00566353	ppopah - Tptpm	Tsw2	B	085, 88N		normal dip separation				
ESF 43+39	SPC00530198, SPC00543700	ppopah - Tptpm	Tsw2	B	160, 84W	160, 00; 170, 59*		3 cm, 10 cm max	USGS SPC005412 97, related fractures: 200, 72W; 160,00 set predates 170, 59 set		Fig. 7a and c; 8a and b; Fig. 15
ESF 53+80	SPC00552526	ppopah - Tptpm	Tsw2	B	330, 74W	240, 74	normal dip separation				
ESF 53+86	SPC00552525	ppopah - Tptpm	Tsw2	B	215, 82W	031, 29		1.5 cm			
ESF 54+73.5	SPC00552524	ppopah - Tptpm	Tsw2	B	133, 72S				at intersection with fault 235, 85E, norm sep.		Fig. 7b

Table 1. Fault and Related Feature Data.

ESF 54+80.5	SPC00552522, SPC00552523	ppopah - Tptpm	Tsw2	B	053, 84N		2.5 cm normal dip				
ESF 60+44	SPC00552516, SPC00552517	ppopah - Tptpm	Tsw2	B	348, 80W		0.5 m reverse dip	2 cm, 5 cm max.	field photos		
ESF 67+46.5	SPC00552515	Tiva - Tpcpln	TCw	B	125, 81W	166, 76	8 cm normal dip	2.5 cm	field photos		
ESF 75+90	none	Tiva - Tpcpln	TCw	B	000, 81W	315, 78	30 cm right lateral strike separation and 45 cm normal dip separaton	3.5 cm core, no measurable damag ezone	non-Q sample , confirmed Class B fault, joint 095, 70N appears offset by fault		
ESF 76+11.5	SPC00534018	Tiva - Tpcpmn	TCw	B	340, 80W		15 cm dip separation, 45 cm right-lateral strike separation	5.5 cm, 18 cm max			
ESF 76+12.4	SPC00543704	Tiva - Tpcpmn	TCw	B	343, 70W				same fault as ESF 76+11.5 but higher in ESF		
ESF 76+17	SPC00543701, SPC00543702, SPC00543703, SPC00534017	Tiva - Tpcpmn	TCw	B	167, 74W; 347, 70W; 356, 74W		norm dip	5 cm, 10 cm max.	USGS SPC005412 98		C and O isotopic analysis; Fig. 6 and 16.
ESF 35+92.5	SPC00566352, SPC00552529. SPC00552528, SPC00552527	ppopah - Tptpm	Tsw2	C	352, 81W; 345, 81W	352, 00; 344, 07			Sundance; field photos	**2840**; "fault breccia"	Fig. 8c and d; Fig. 10a
ESF 62+08	SPC00534022, SPC00534023	ppopah - Tptpm	Tsw2	C	307, 82S	low and high plunge					
ESF 62+09	SPC00552521	ppopah - Tptpm	Tsw2	C	140, 80W	230, 80; 140, 00; 146, 29	right lateral strike separation and normal dip				
ESF 62+70	SPC00552520	ppopah - Tptpm	Tsw2	C	324, 87E	326, 35		7 cm			

24/57

Table 1. Fault and Related Feature Data.

ESF 63+22.5	SPC00552518, SPC00552519	opopah - Tptpu	TSw1	C	342, 53W	252, 53	normal dip separation	10 cm, 15 cm max			
ESF 76+09	SCP00534019	Tiva - Tpcpmn	TCw	C	198, 75W	288, 75					
ESF 76+47	SPC00534001A	Tiva - Tpcpmn	TCw	C							
ESF 76+76.2	SPC00534000	Tiva - Tpcpmn	TCw	C	010, 69W					334 - 445; "breccia"	
ECRB 4+99	SPC00552507	opopah - Tptpu	TSw1	C	211, 64N			4 cm, 25 cm max; 2 m damage zone	left rib Ghost Dance?		
ECRB 11+35	SPC00566360	opopah - Tptpm	Tsw2	C					Sundance		
ECRB 11+35.4	SPC00552506	opopah - Tptpm	Tsw2	C	279, 70N	279,00			Sundance		
ECRB 11+35.5	SPC00566359	opopah - Tptpm	Tsw2	C	271, 80 N	271, 00		30 cm	Sundance		
ECRB 25+37.36	SPC00543709	opopah - Tptpl	TCw	C	013, 80W				fault		
Alcove 5 01+00	none			C	200, 08W	030, 08	reverse dip separation		thrust		
alcove 6 00+36	SPC00530197			C	012, 87W	198, 65*	l.l. strike slip, norm dip slip	3 cm			
Alcove 6 00+74	none			C	012, 28E		reverse dip slip		thrust, cut across by normal fault: 000,		
alcove 6 00+84	SPC00543705			C	124, 14E		reverse dip separation		thrust		
alcove 6 00+85.5	SPC00534025			C			reverse dip slip		thrust		Fig. 9
alcove 6 00+97	SPC00530195			C	170, 71W			1.4m	Sundance		
Alcove 6 01+23.1	none			C	285, 46N	015, 46	reverse dip slip		thrust		
alcove 6 01+52	SPC00530196; SPC00534024			C	200, 83W; 024, 90		normal separation		Ghost Dance		Fig. 10b
ESF 67+84.9	SPC00552512, SPC00552511, SPC00552510	Tiva - Tpcpln	TCw	D	164, 74W	221, 71	7 m minimum normal dip separation	30 cm, 5 cm damage zone	Dune Wash Western Splay		
ESF 67+85.2	SPC00534021	Tiva - Tpcpln	TCw	D	148, 85W		normal dip separation		Dune Wash		
ESF 67+87.2	SPC00534020	Tiva - Tpcpln	TCw	D					Dune Wash; field	475; "fault/grabe	
ESF 67+89	SPC00552513, SPC00552514	Topopah - Tptrn	TSw1	D	355, 63W	275, 62			Dune Wash Eastern Splay; field photos		

Table 1. Fault and Related Feature Data.

ECRB 25+84.8	SPC00552500	opopah - Tptpl	TCw	D	202, 57W		normal dip separation	foliated gouge 6 m, 2 - >8 cm thick	Solitario Canyon		
ECRB 25+85.1	SPC00543706, SPC00543707	opopah - Tptpl	TCw	D	190, 60W; 193, 50W				Solitario Canyon		XRD analysis; Fig 12; Fig. 13
ECRB 25+85.5	SPC00552501	opopah - Tptpl	TCw	D	201, 65W				Solitario Canyon		
ECRB 25+86.0	SPC00552502	opopah - Tptpl	TCw	D			norm dip separation		Solitario Canyon		
ECRB 25+86.2	SPC00552503	opopah - Tptpl	TCw	D					Solitario Canyon		
ECRB 25+86.3	SPC00543708	opopah - Tptpl	TCw	D	188, 58W				Solitario Canyon		
ECRB 25+87.5	SPC00552504	opopah - Tptpl	TCw	D					Solitario Canyon		
ESF 16+12.4	SPC00566369	Topopah - Tptrr	TSw1	na						382; "cooling joint"	
ESF 16+42.65	SPC00566365, SPC00566366	Topopah - Tptrr	TSw1	na	286, 90	286, 80	normal dip separation	4 cm	sheared cooling joint, no		
ESF 16+44	SPC00566367	Topopah - Tptrr	TSw1	na					cooling joint with foliated gouge, no		
ESF 24+37.5	SPC00530192, SPC00530193	opopah - Tptpu	TSw1	na	040, 80E	041, 06; 059, 62; 130, 80 (HW up) ; 210, 43*			cooling joint; 130,80 slickenlines predate 058,60 set		
ECRB 20+87	SPC00543710	Topopah - Tptp	Tsw2	na					mineralized lithophysal cavity		
ESF 15+05.7	none	Topopah - Tptrr	TSw1	?					135, 82S terminates against 207, 74W		
ESF 16+02	SPC00566370	Topopah - Tptrr	TSw1	?					Sample insufficient to classify		
ESF 16+58.5	SPC00566364	Topopah - Tptrr	TSw1	?	214, 85W		normal dip separation		no section		

Table 1. Fault and Related Feature Data.

ESF 19+28.5	SPC00566361	opopah - Tptpu	TSw1	?	321, 76W	321, 00		15 cm , 30 cm max	Drill Hole Wash B, left rib		
ESF 19+42	SPC00530190, SPC00530191	opopah - Tptpu	TSw1	?	160, 85E				Drill Hole Wash B, field photos, offsets a Class B fault (330, 74W, with dip slicks)	**2290;** "breccia"	
ESF 53+80	none	ppopah - Tptpm	Tsw2	?	068, 90	vert slicks	normal dip separation				
ESF 59+75	none	ppopah - Tptpm	Tsw2	?	212, 69W	302, 69	reverse dip separation		this fault offsets 320, 85E by 10 cm.		
ESF 59+84	none	ppopah - Tptpm	Tsw2	?					325 striking r.l. faults offset 065 striking faults		
ESF 67+76.4	none	Tiva - Tpcpln	TCw	?	142, 79W	142,00					
ESF 75+35	none	Tiva - Tpcpln	TCw	?	339, 78W	249,78		9 cm core, 15 cm maximum			
ESF 75+62.8	none	Tiva - Tpcpln	TCw	?	058, 71W			3 cm core			
ESF 75+74.7	none	Tiva - Tpcpln	TCw	?	002, 73W		2.5 cm dip separation, left-lateral strike separation	2 cm core, 4 cm max, no measurable damage zone	class B confirmed in the field only		
ESF 75+78	none	Tiva - Tpcpln	TCw	?	342, 73W			6 cm core, 7.5 cm damage zone		418; "breccia"	
ESF 75+89	none	Tiva - Tpcpln	TCw	?	005, 79W		normal dip separation	15 cm			
ECRB 13+16.5	none	ppopah - Tptpm	Tsw2	?	345, 90	345, 00	strike slip				

31/57

Table 1. Fault and Related Feature Data.

ECRB 13+17	none	ppopah - Tptpm	Tsw2	?	160, 90	160, 00	strike slip				
ECRB 25+78	SPC00552505	opopah - Tptpl	TCw	?					no section		

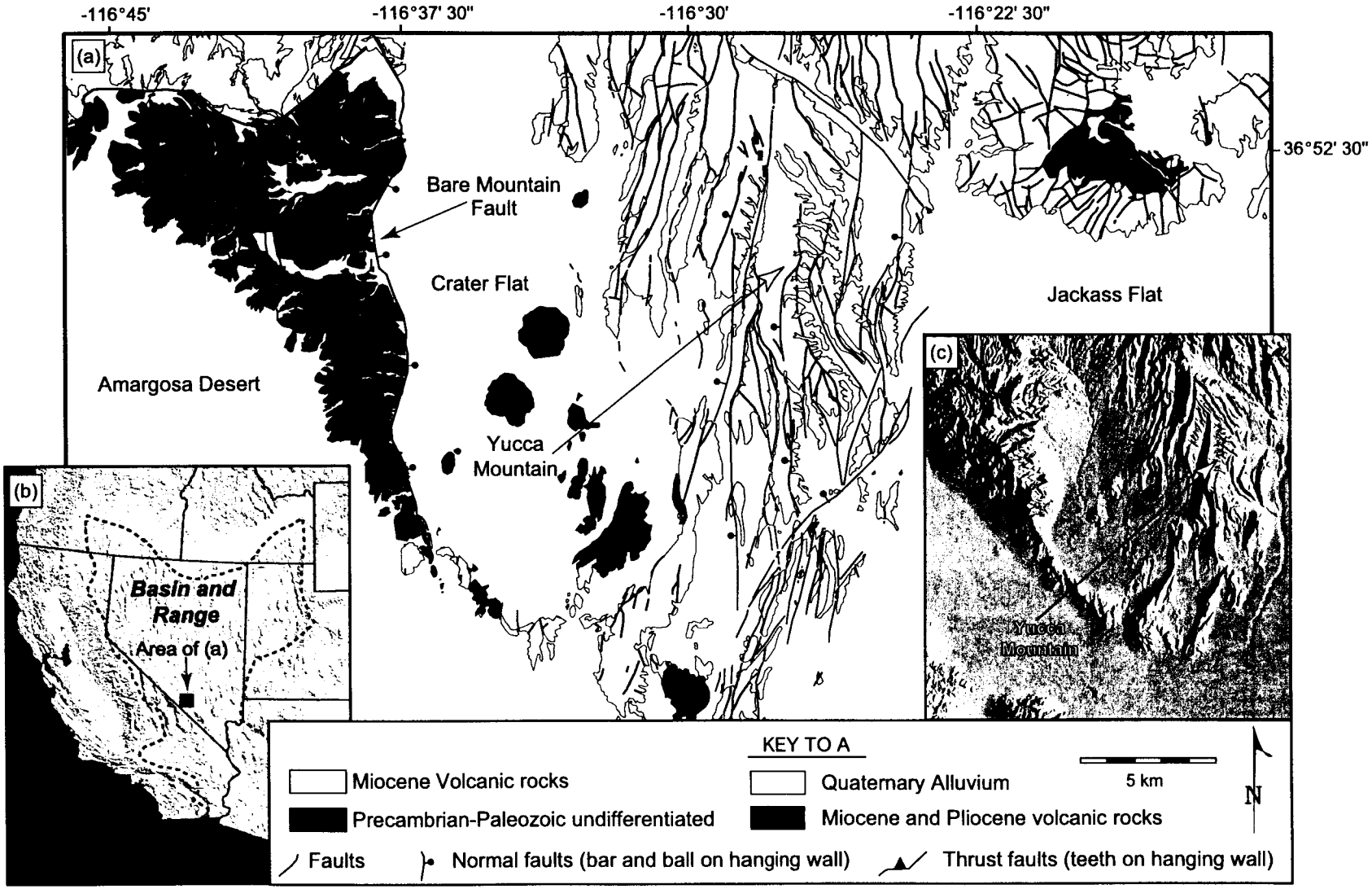

Figure 1
Gray et al., 2001

33/51

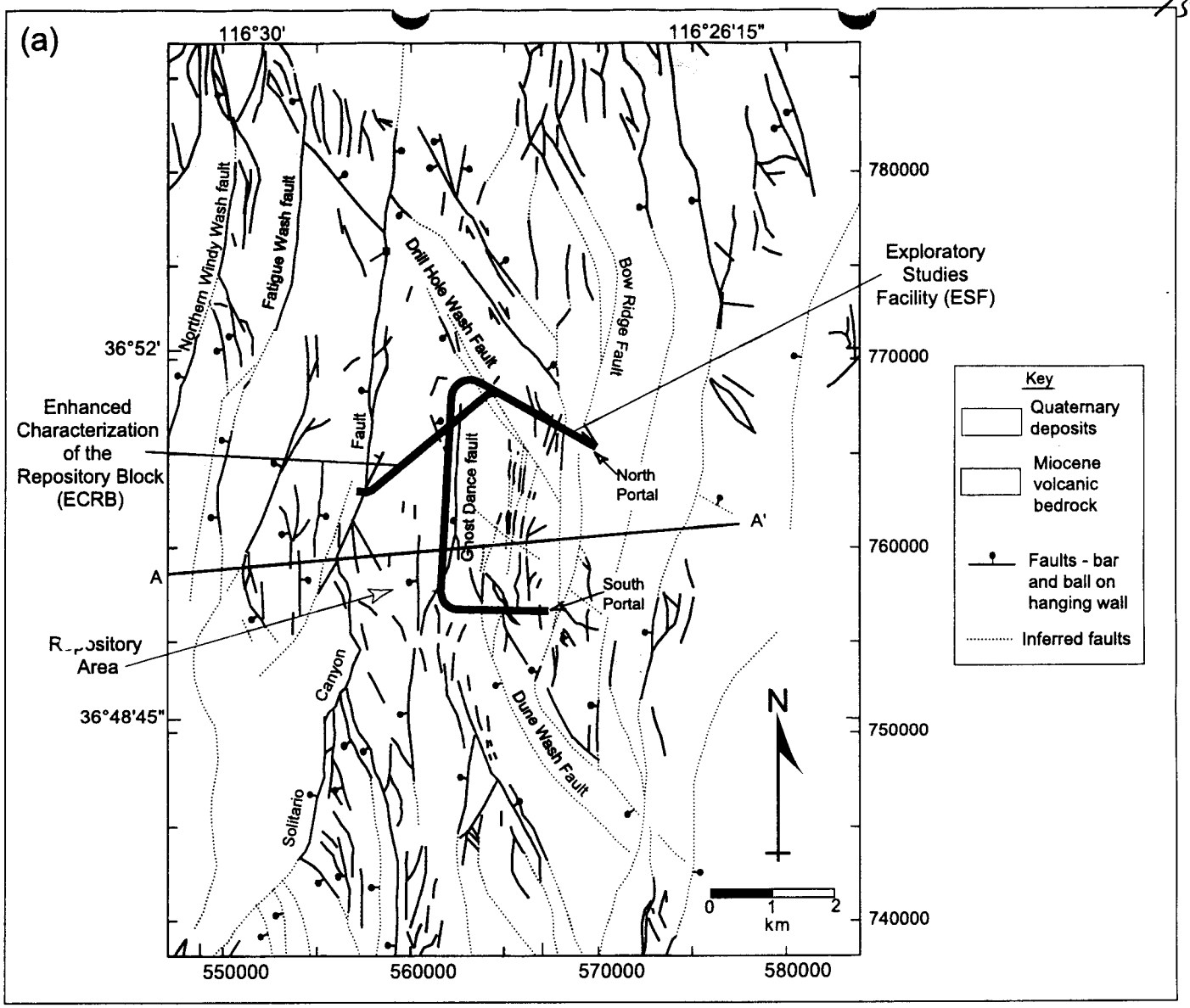

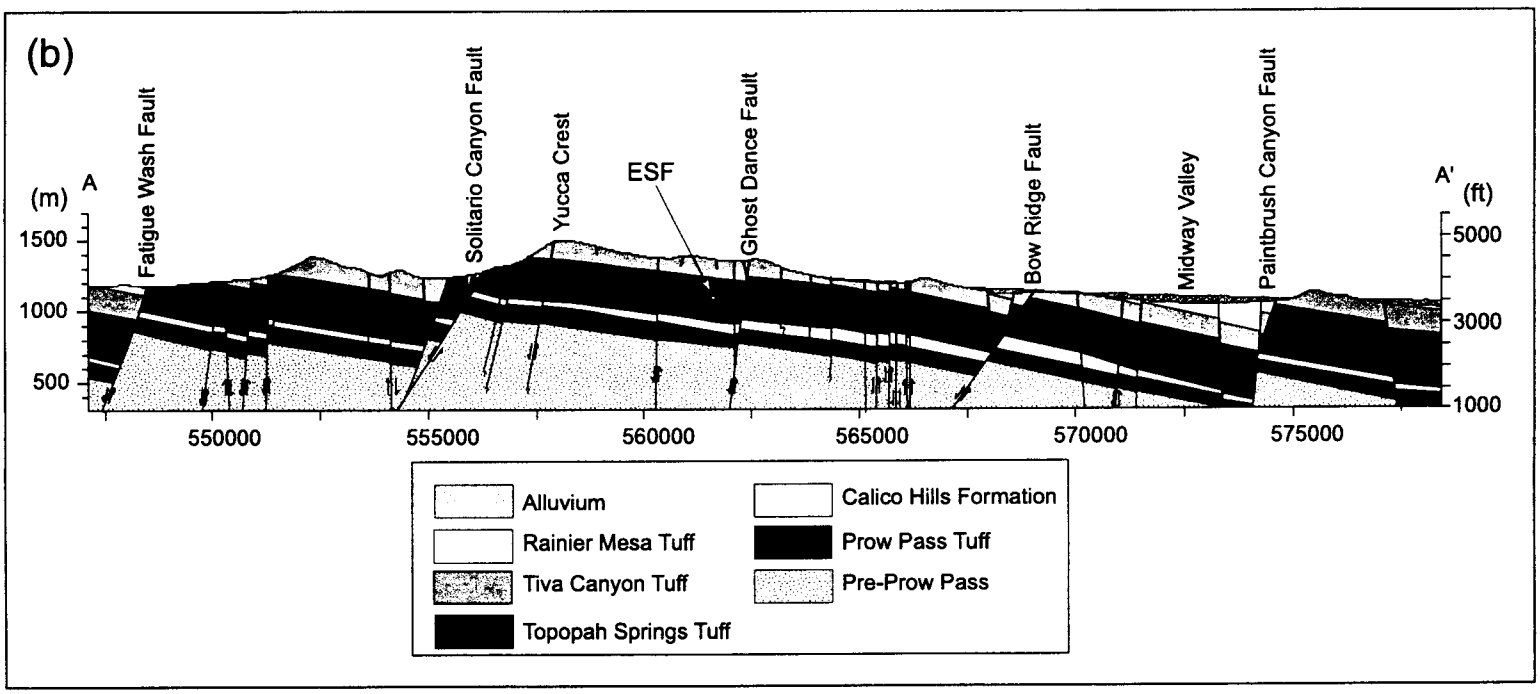

Figure 2
Gray et al., 2001

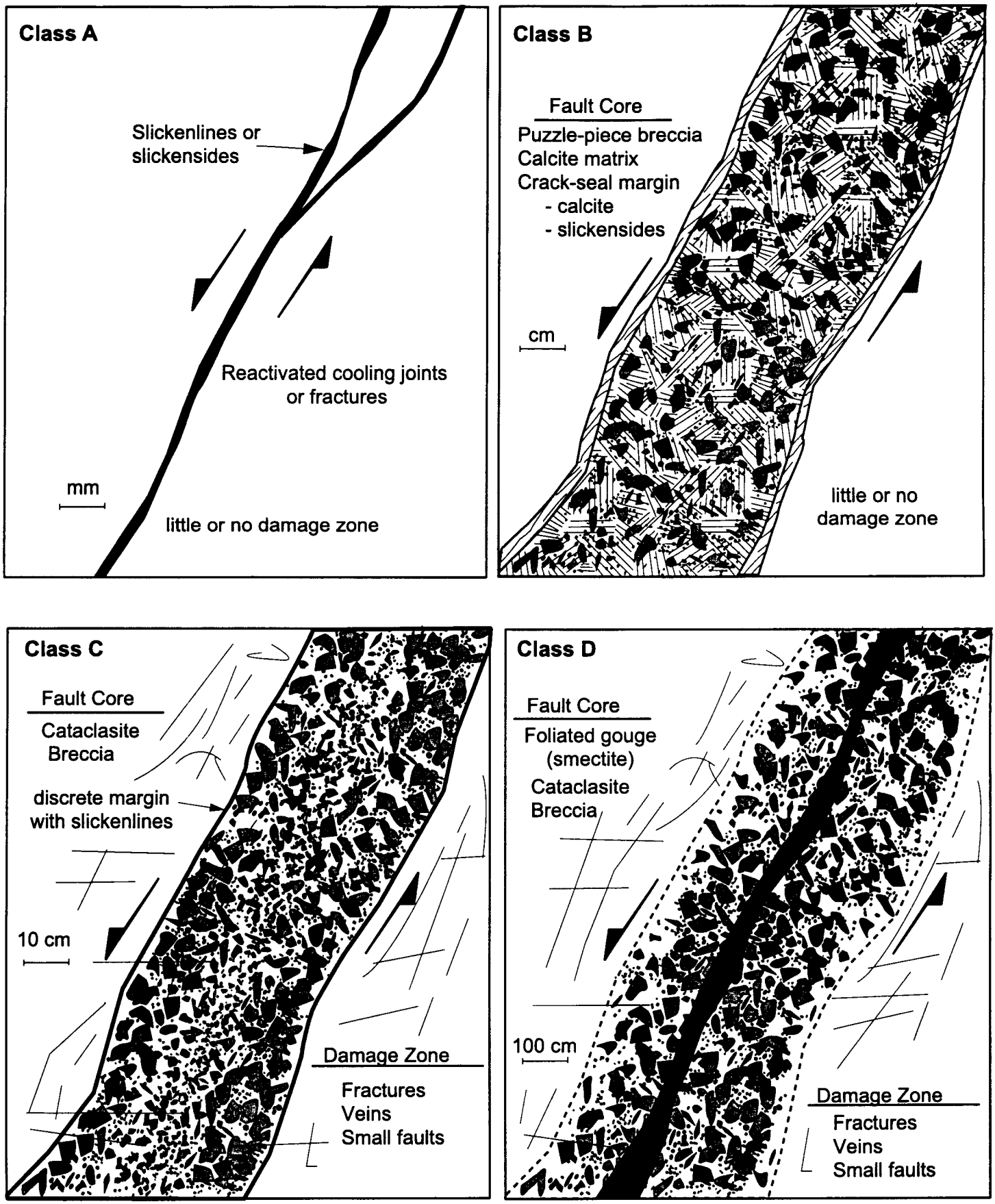

Figure 3
Gray et al., 2001

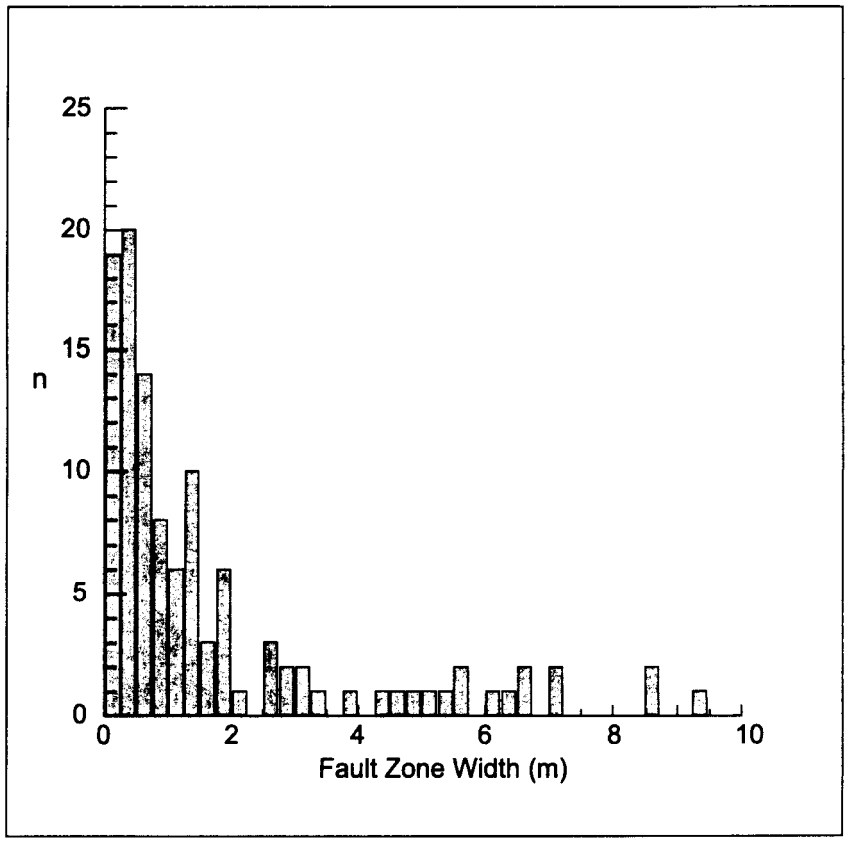

Figure 4
Gray et al., 2001

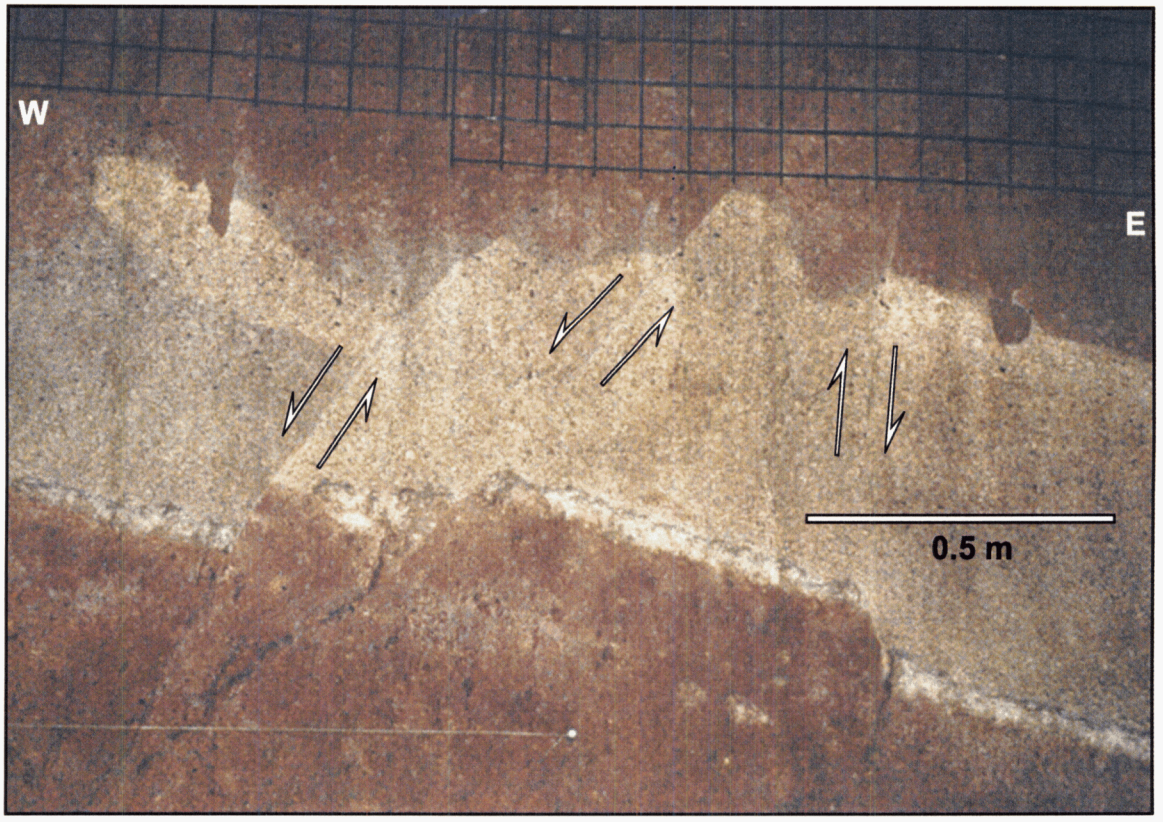

Figure 5
Gray et al., 2001

Figure 6
Gray et al., 2001

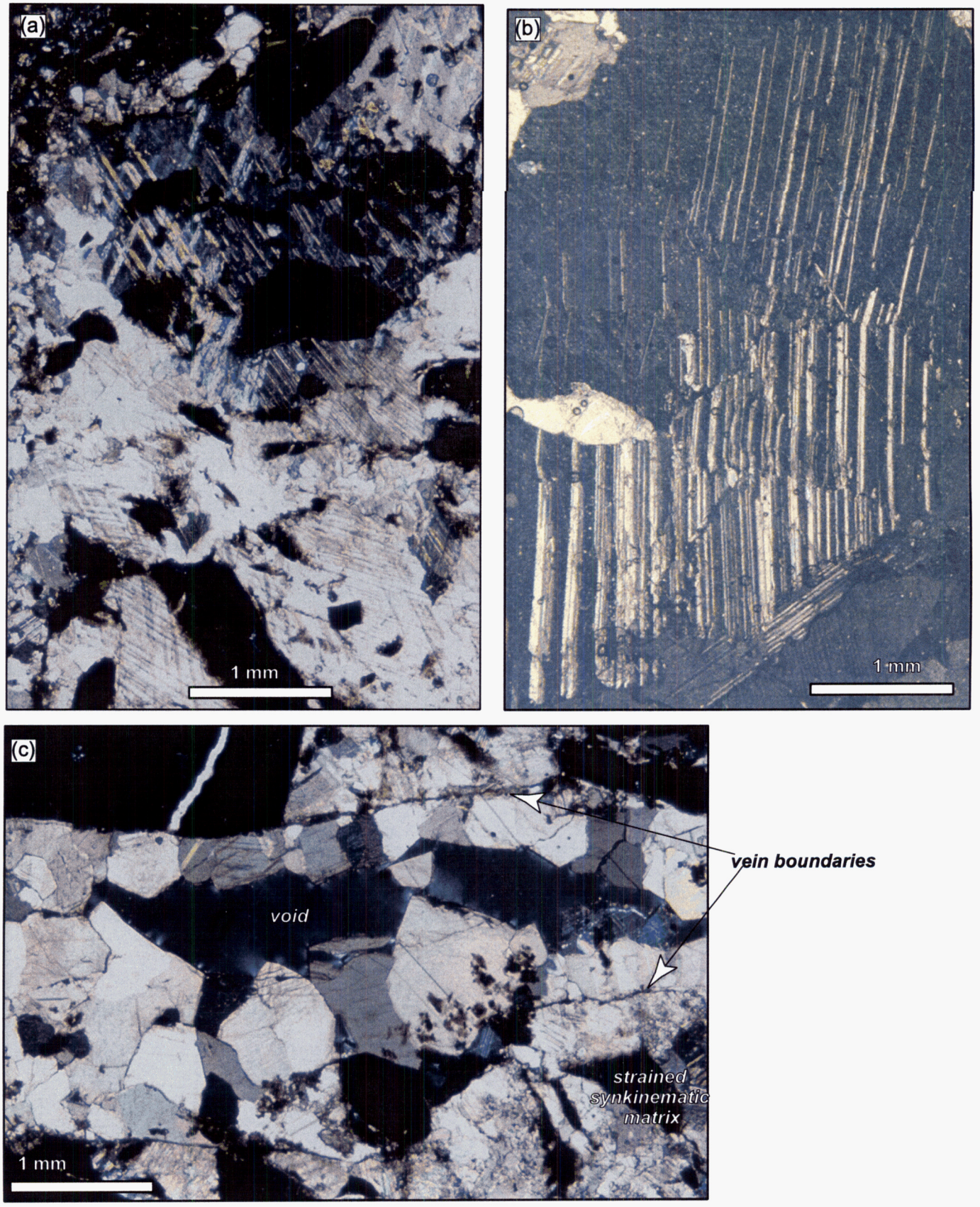

Figure 7
Gray et al., 2001

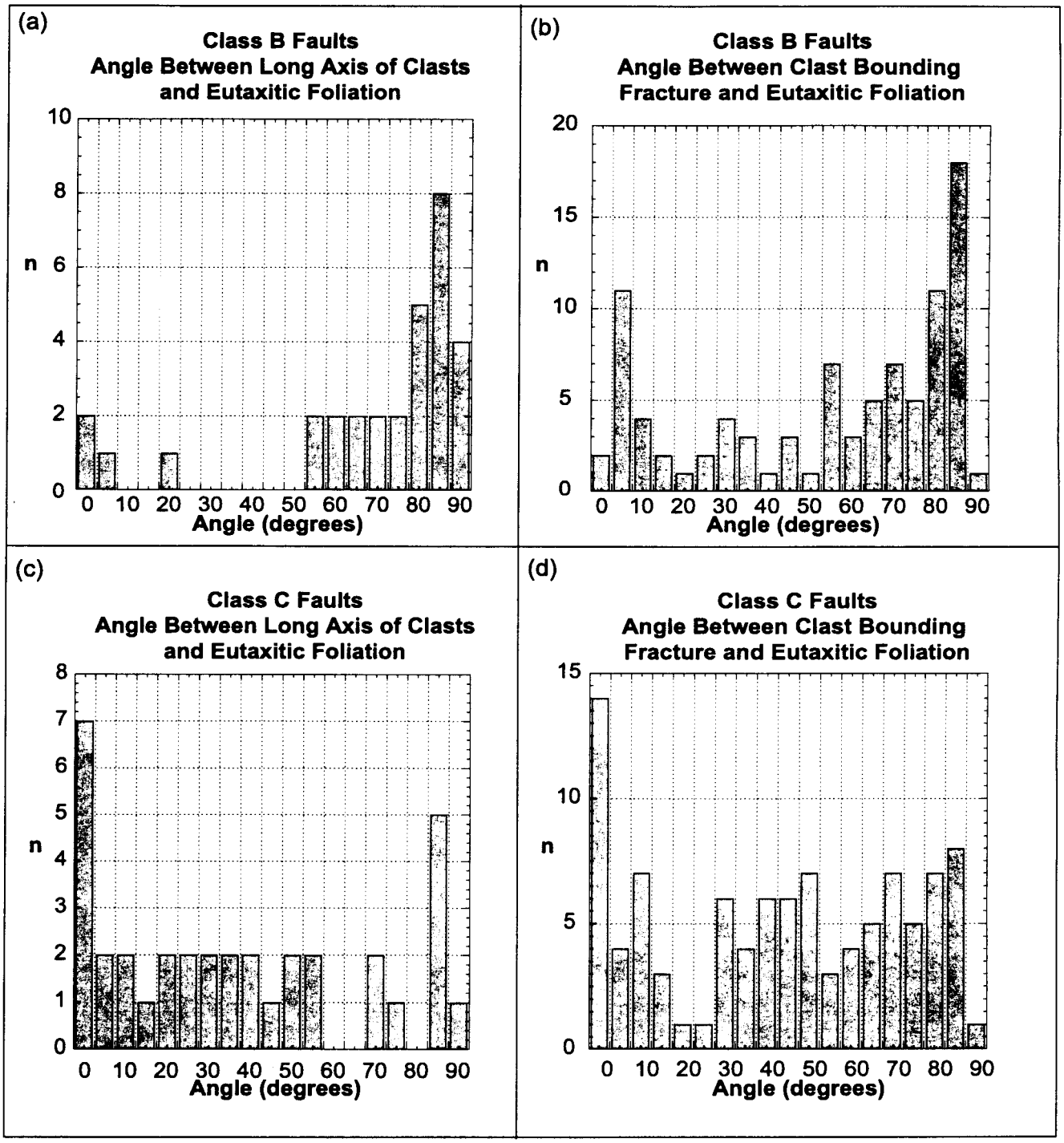

Figure 8
Gray et al., 2001

Figure 9
Gray et al., 2001

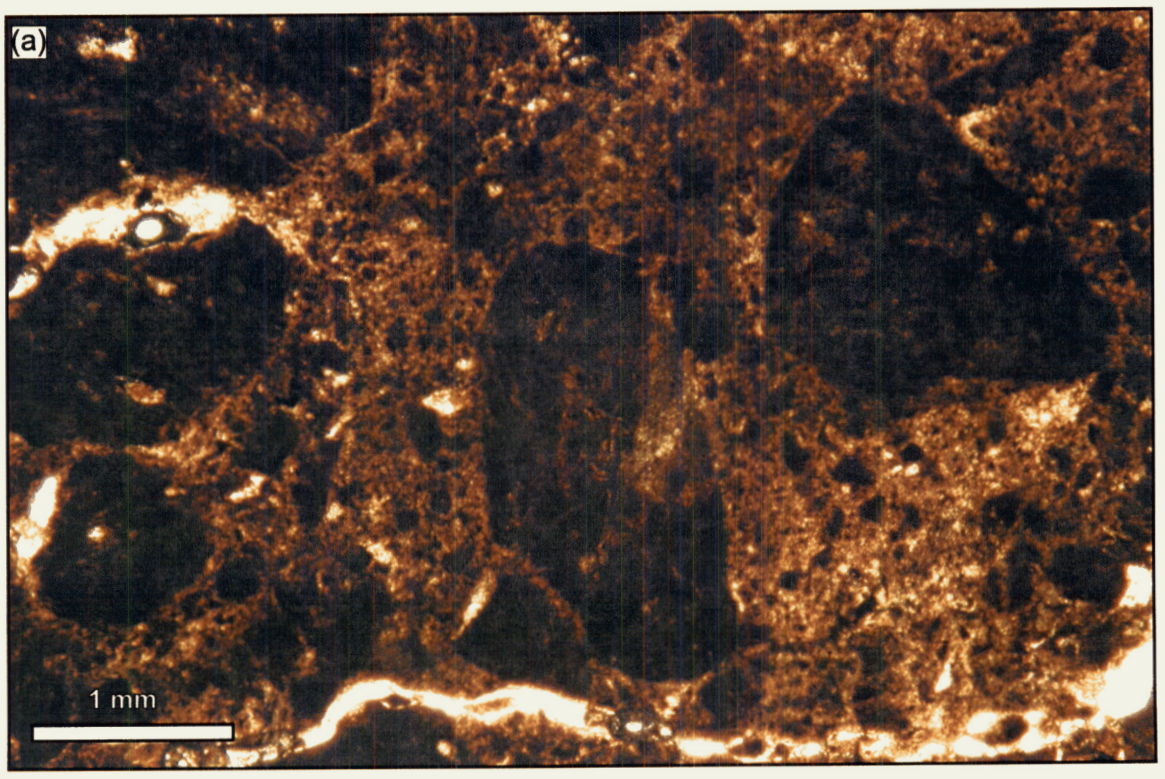

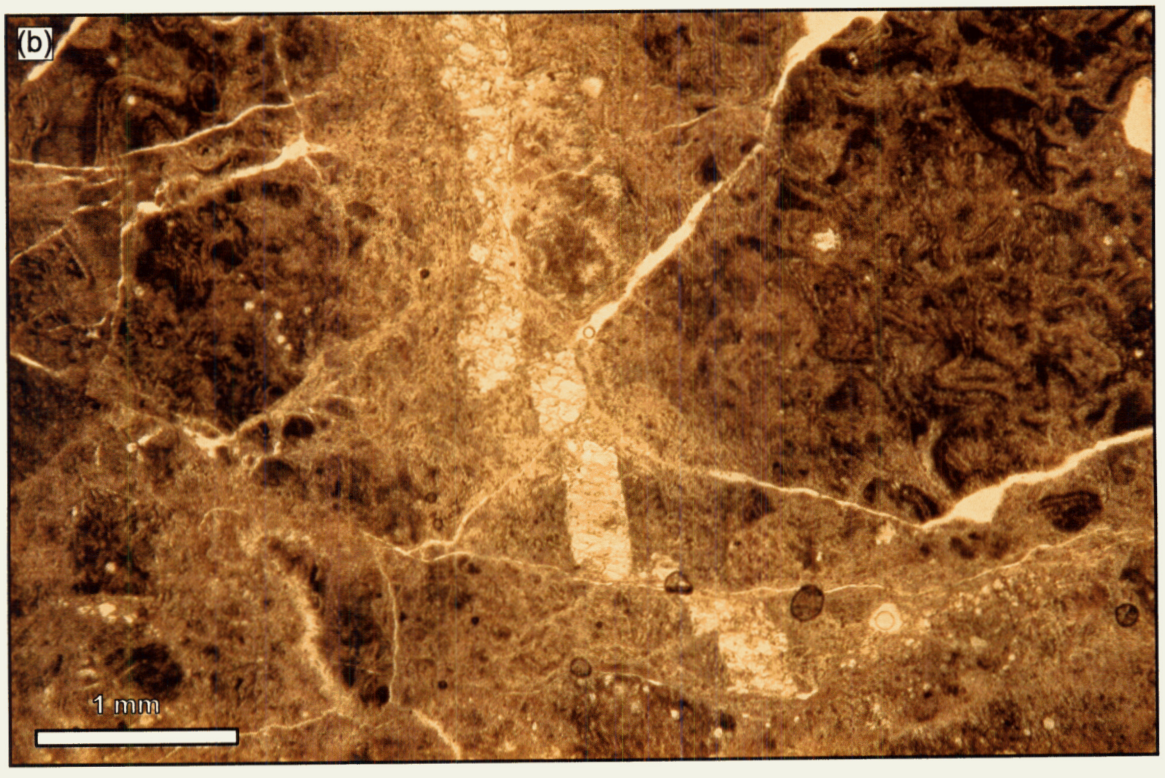

Figure 10
Gray et al., 2001

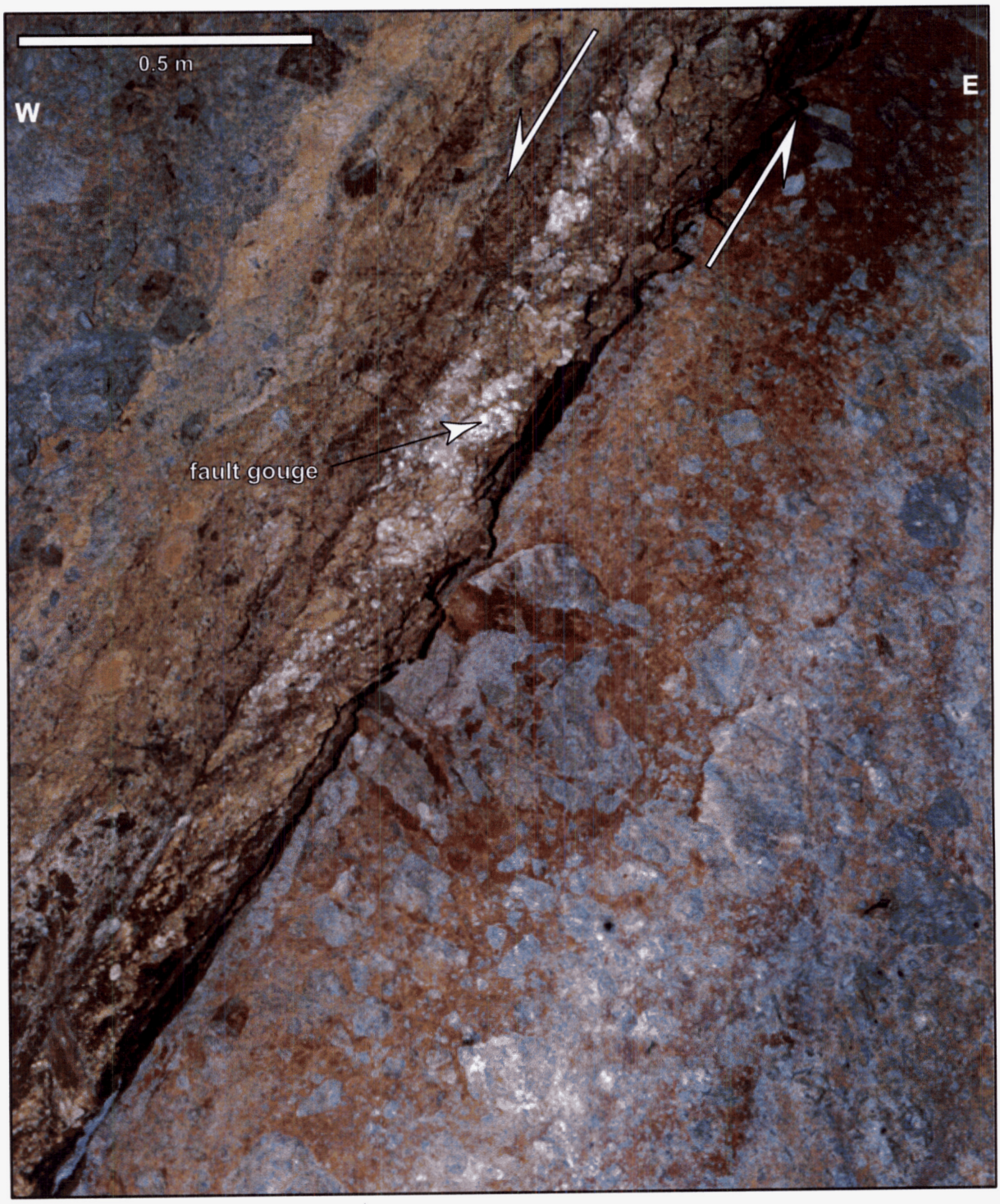

Figure 11
Gray et al., 2001

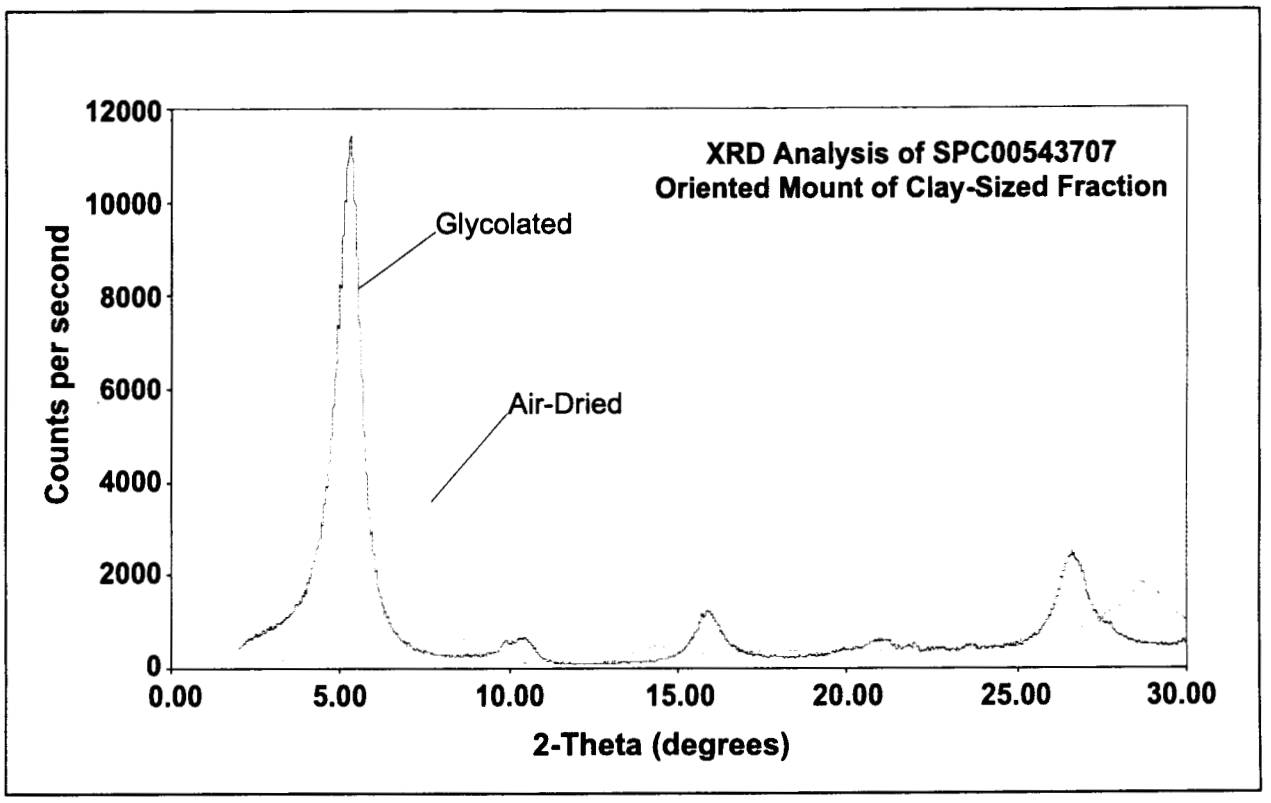

Figure 12
Gray et al., 2001

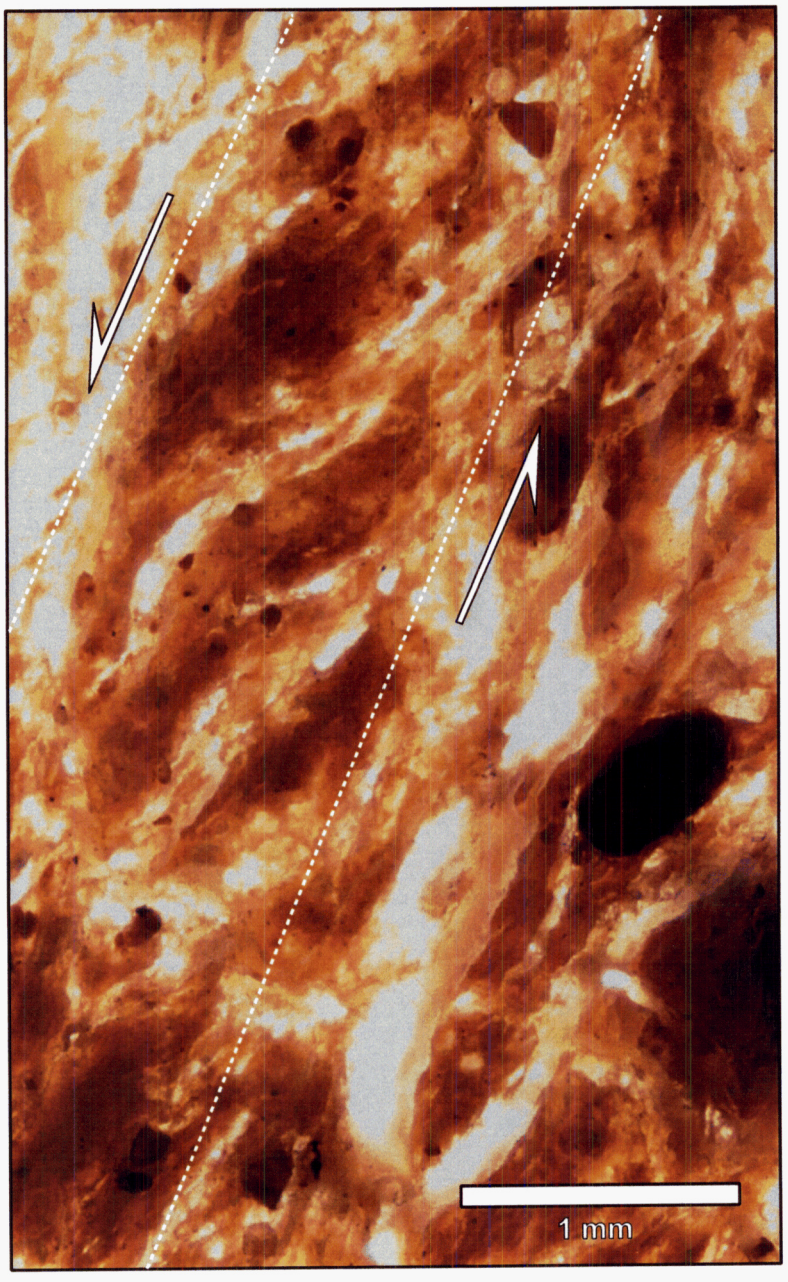

Figure 13
Gray et al., 2001

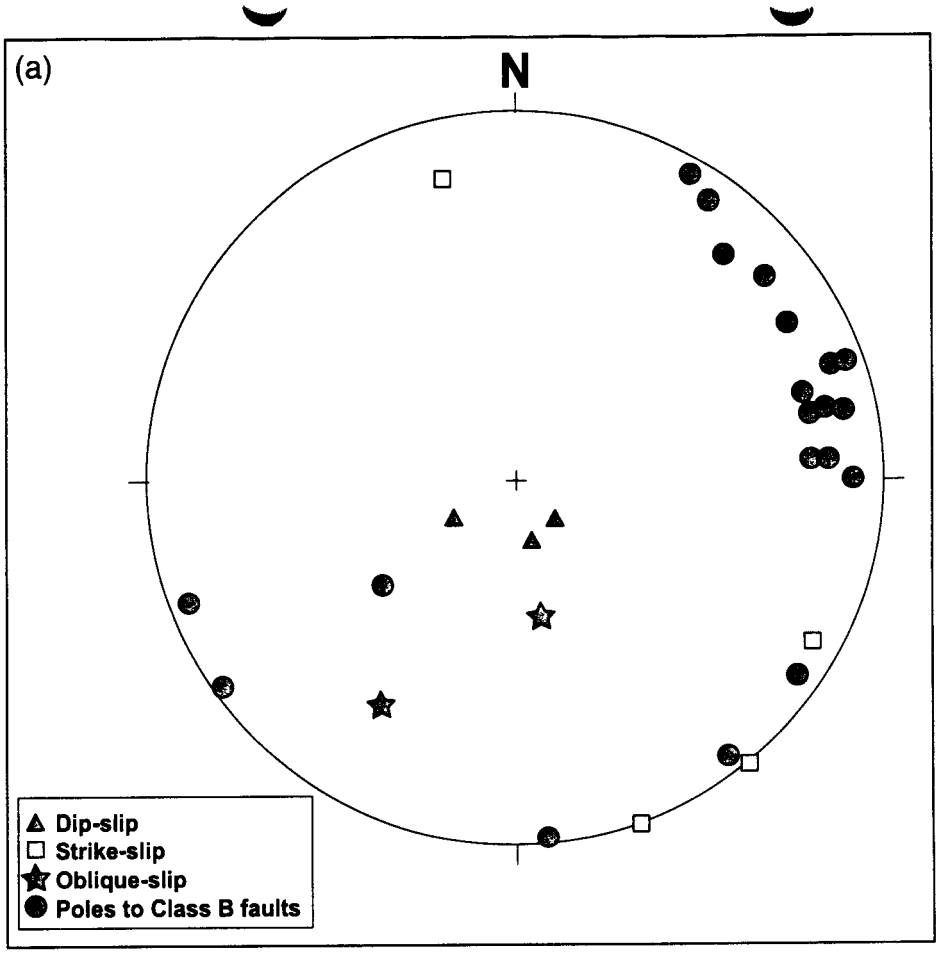

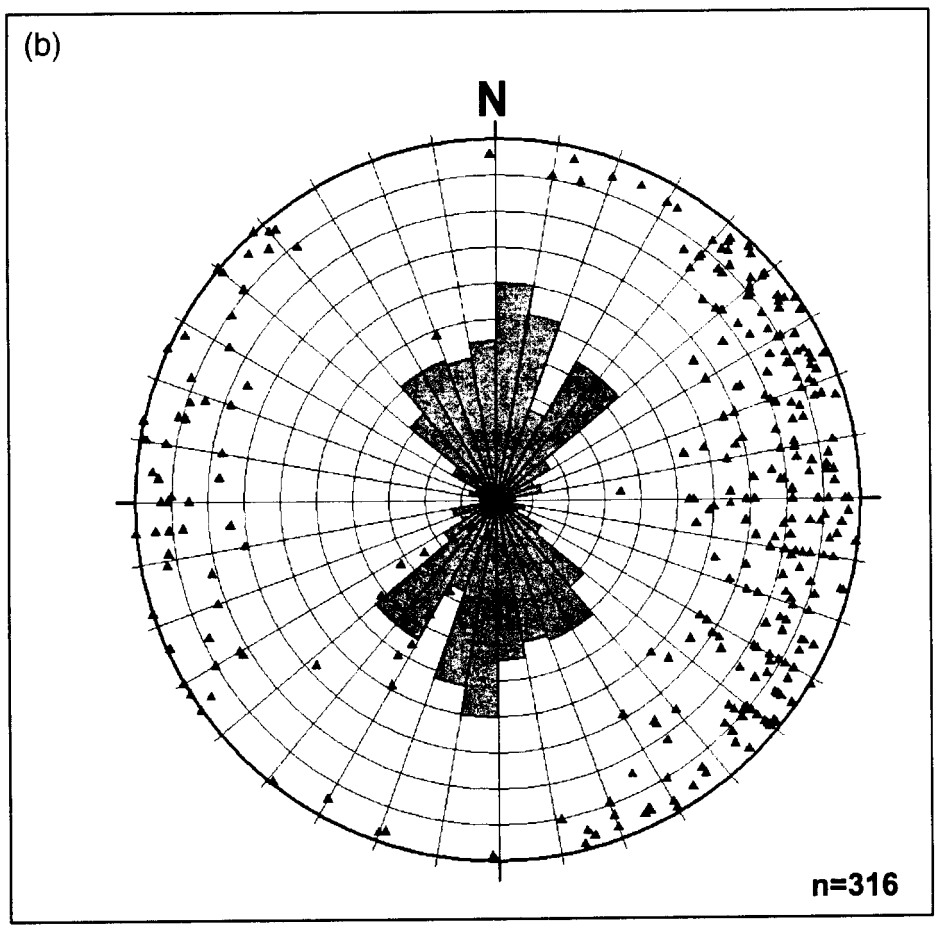

Figure 14
Gray et al., 2001

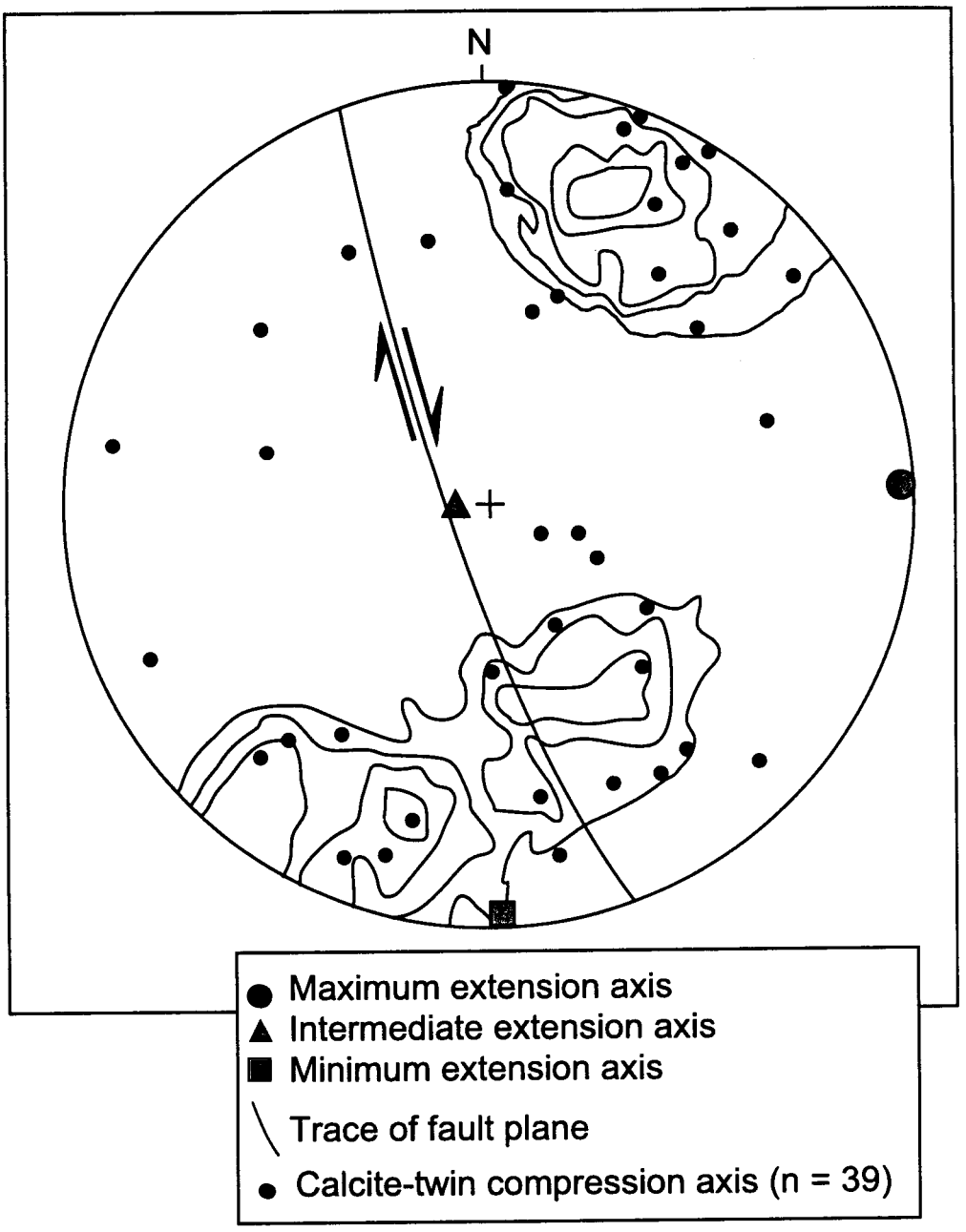

Figure 15
Gray et al., 2001

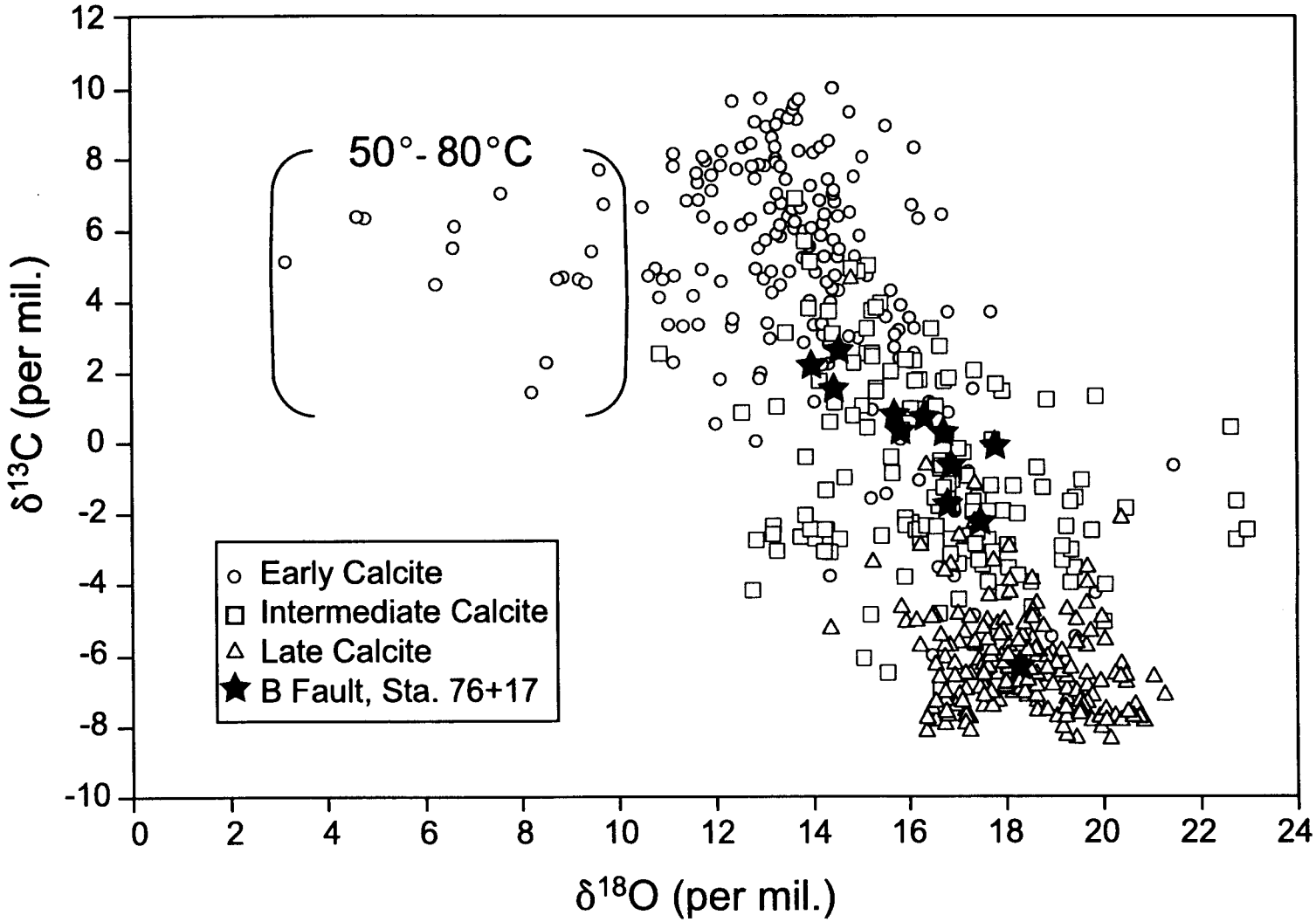

Figure 16
Gray et al., 2001

15/84

Figure Captions

Figure 1. Location and geologic setting of a potential Yucca Mountain high-level radioactive waste repository within the Basin and Range physiographic province. Geology in (a) is from Frizzell and Schulters (1990) and Day et al. (1998). Digital elevation models in (b) and (c) are from the USGS Digital Line Graph Data Set.

Figure 2. (a) Geologic map and (b) cross section of Yucca Mountain showing the location of the Exploratory Studies Facility and Cross Drift relative to mapped faults. Map and cross section are modified from Day et al., (1998). Site coordinates are latitude- longitude and Universal Transverse Mercator, zone 11.

Figure 3. Illustration of the main features in each of the four classifications of fault zones observed in the Exploratory Studies Facility and Cross Drift at Yucca Mountain, Nevada.

Figure 4. Fault width data for faults mapped in the Exploratory Studies Facility (ESF). The fault data are from the 112 fault zones identified in the data set that have recorded fault-zone widths. Fault data are the Exploratory Studies Facility data transmitted from the U.S. Department of Energy to the Center for Nuclear Waste Regulatory Analyses, August, 1998, U.S. Department of Energy Data Tracking Number numbers GS960708314224.008, .101, .011, .014, .003, .008, .010, .012, .020, .021, .022, .023, .024, .025, .026, and .028; Technical Data Information Form numbers 305556, 305554, 305624, 306645, 306017, 306284, 306298, 306299, 306509, 306510, 306511, 306512, 306513, 306514, 306515, 306516, 306517.

Figure 5. Gently east-dipping non-welded tuff (PTn) is offset by conjugate Class A faults.

Figure 6. South-looking photograph of a Class B fault at ESF station 76+17.8. Heavily mineralized fault core has well-defined slickensided boundaries flanked by an intensely fractured, relatively narrow damage

zone. Hammer for scale. Isotopic data collected from calcite matrix material at this site is presented in Fig. 16.

Figure 7. Class B fault photomicrographs taken in crossed polarized light. (a) Abundant calcite matrix from a sample at ESF station 43+39 exhibits characteristic poikilotopic texture. Calcite strain gauge data collected from this fault is presented in Fig. 15. (b) Calcite crystals contain intra- and intercrystalline fractures along which sliding has taken place. Sample from station 54+73.5. (c) A post-kinematic vein transects strained calcite matrix in a sample from ESF station 43+39.

Figure 8. Data on the effect of primary anisotropy on the orientation of the long axis of clasts and the clast bounding fractures in a Class B fault core (SPC00530198G at station 43+39) (a) and (b) respectively, and a Class C fault from SPC 00552529B at station ESF 35+92.5 (the Sundance Fault) (c) and (d) respectively. (a) Most clasts are elongate sub-perpendicular to the eutaxitic foliation, indicating that Class B faults did not undergo significant clast comminution and the faults initiated by rupture at a high angle to layering. (b) Most clasts are bounded by fractures at high angles to the eutaxitic foliation. (c) Class C faults underwent more comminution than Class B faults resulting in more clasts with long axes sub-parallel to the eutaxitic foliation. (d) Fractures sub- parallel to the eutaxitic foliation (primary anisotropy) are most common and other orientations are evenly distributed, indicating comminution of wall rock clasts by cataclastic flow.

Figure 9. Class C thrust fault zone from Alcove 6 station 00+86, facing south. Chisel for scale.

Figure 10. Plain light photomicrographs from Class C fault cores: (a) Sundance fault, SPC00552529B (ESF station 35+92.5); (b) Ghost Dance fault, SPC00534024A (alcove 6), showing shearing of core and chalcedony vein.

Figure 11. North looking photograph of the Solitario Canyon fault core. Foliated smectitic gouge is surrounded by breccia with patchy opal/calcite mineralization and oxidized matrix.

Figure 12. XRD data patterns from the clay-sized fraction of the Solitario Canyon Fault Gouge (SPC00543707). Oriented sample was analyzed in both air-dried and ethylene glycol- saturated conditions. Peak shift of glycol-treated sample towards lower 2 values (higher d-spacing) indicates the presence of smectite in the fault gouge.

Figure 13. Solitario Canyon fault gouge (SPC00543706B) with sigmoidal P-foliation is asymptotic into shear planes sub-parallel to shear zone boundary. Photomicrograph is in plain light and long dimension is 5 mm. Asymmetry is consistent with hanging wall down-to-the-west sense of shear.

Figure 14. (a) Class B faults traces and slickenlines are plotted on a lower hemisphere, equal area projection. Most Class B faults contain dip-slip lineations, strike NW-SE, and dip steeply to the SW. (b) Rose diagram (plot radius = 10%) of fault orientations mapped in the Exploratory Studies Facility (ESF). Fault data the 316 faults identified in the Exploratory Studies Facility data transmitted from the U.S. Department of Energy to the Center for Nuclear Waste Regulatory Analyses, August, 1998, U.S. Department of Energy Data Tracking Number numbers GS960708314224.008, .101, .011, .014, .003, .008, .010, .012, .020, .021, .022, .023, .024, .025, .026, and .028; Technical Data Information Form numbers 305556, 305554, 305624, 306645, 306017, 306284, 306298, 306299, 306509, 306510, 306511, 306512, 306513, 306514, 306515, 306516, 306517.

Figure 15. Calcite strain gauge data from mutually perpendicular thin sections (SPC00530198F and G from station 43+39) indicates principal strain axis consistent with right-lateral strike slip deformation in the calcite matrix.

Figure 16. U. S. Geological Survey C and O stable isotope data with data from Class B calcite matrix at ESF station 76+17 for comparison. Class B calcite matrix is chemically similar to intermediate to late stage calcite in lithophysae and fractures in the ESF/ECRB.